

SURFACE WAVE TOMOGRAPHY OF THE UPPER MANTLE BENEATH THE  
REYKJANES RIDGE

A THESIS SUBMITTED TO THE GRADUATE DIVISION OF THE UNIVERSITY  
OF HAWAI'I IN PARTIAL FULFILLMENT OF THE REQUIREMENTS FOR THE  
DEGREE OF

MASTER OF SCIENCE

IN

GEOLOGY AND GEOPHYSICS

MAY 2006

By  
Andrew A. Delorey

Thesis Committee:

Robert A. Dunn, Chairperson  
Garrett Ito  
John M. Sinton  
Brian Taylor

We certify that we have read this thesis and that, in our opinion, it is satisfactory in scope and quality as a thesis for the degree of Master of Science in Geology and Geophysics.

THESIS COMMITTEE

---

Chairperson

---

---

---

---

## ACKNOWLEDGEMENTS

All maps are produced using GMT [*Wessel and Smith, 2004*]. Data from the BORG station comes courtesy of the Global Seismograph Network [*Butler et al., 2004*]. All HOTSPOT and ICEMELT data and instrument responses come courtesy of IRIS [*Incorporated Research Institutions for Seismology, 2004*]. Earthquake locations and times are from the International Seismological Centre *Online Bulletin* [*International Seismological Centre, 2001*] and the Engdahl catalog [*Engdahl et al., 1998*]. Earthquake focal mechanisms come from the Harvard CMT Project [*Dziewonski et al., 2004*]. Initial data processing was performed using the software package SAC [*Goldstein, 1996*]. This research was supported by NSF grant OCE03-37237. Eric Mittelstaedt provided mantle flow models used in the interpretation.

## ABSTRACT

This study analyzed broadband records for fundamental mode Love and Rayleigh waves that propagated along the Reykjanes Ridge to study the seismic properties in the upper mantle as it relates to hotspot-ridge interaction. These waves were generated by regional earthquakes occurring in the North Atlantic to the south of Iceland, and were recorded by the HOTSPOT and ICEMELT arrays and the GSN station BORG, located on Iceland. The phase, group, and amplitude information were measured for narrow-pass filtered waveforms over the period range of ~12-100s. Over ~12,000 such measurements were included in an inversion for mantle and lithospheric shear velocity structure; in addition the joint inversion of horizontally polarized Love and vertically polarized Rayleigh wave data solved for mantle seismic anisotropy. Shear wave velocity results show a broad and deep low velocity zone in the upper mantle which is consistent with elevated temperatures and a small degree of partial melt. Shear wave anisotropy results indicate that vertically polarized shear waves are faster than horizontally polarized shear waves in the uppermost mantle within ~200 km of the ridge. This study shows that plume material that spreads out beneath the Reykjanes Ridge from Iceland is not confined to a lithospheric channel beneath the ridge.

## TABLE OF CONTENTS

ACKNOWLEDGEMENTS.....	III
ABSTRACT.....	IV
LIST OF TABLES.....	VII
LIST OF FIGURES.....	VIII
LIST OF FIGURES.....	VIII
LIST OF ABBREVIATIONS.....	IX
LIST OF ABBREVIATIONS.....	IX
CHAPTER 1. INTRODUCTION.....	1
CHAPTER 2. STUDY AREA.....	3
CHAPTER 3. DATA.....	7
CHAPTER 4. METHODS.....	9
CHAPTER 5. RESULTS.....	15
TABLE 1. SHEAR WAVE STARTING MODEL.....	31
FIGURE 1. REYKJANES RIDGE WITH EVENTS AND STATIONS.....	32
FIGURE 2. LOVE AND RAYLEIGH WAVE GROUP VELOCITIES.....	33
FIGURE 3. RAYLEIGH WAVE ENERGY FOCUSING.....	34
FIGURE 4. LOVE WAVE ENERGY FOCUSING.....	35
FIGURE 5. PHASE VELOCITIES.....	36
FIGURE 6. ALONG AXIS VELOCITY VARIATIONS.....	37
FIGURE 7. EFFECTS OF ICELAND ON SURFACE WAVES.....	38
FIGURE 8. SHEAR WAVE VELOCITY AND ANISOTROPY.....	39
FIGURE 9. SHEAR WAVE VELOCITY UNCERTAINTIES.....	40
FIGURE 10. TEMPERATURE AND MELT.....	41
FIGURE 11. GRAVITY.....	42
FIGURE 12. PASSIVE FLOW BENEATH A MIGRATING RIDGE.....	43
FIGURE 13. MANTLE FLOW BENEATH THE REYKJANES RIDGE.....	44
APPENDIX A. EARTHQUAKE RADIATION PATTERNS.....	45
APPENDIX B. INSTRUMENT RESPONSE.....	47
APPENDIX C. SIGNAL PROCESSING.....	48

	vi
APPENDIX D. INVERSE PROBLEM.....	51
TABLE A-1. ICEMELT EVENT PARAMETERS.....	53
TABLE A-2. HOTSPOT EVENT PARAMETERS.....	54
TABLE A-3. BORG EVENT PARAMETERS.....	55
TABLE B-1. INSTRUMENT LOCATIONS AND TYPES .....	56
TABLE B-2. INSTRUMENT POLES AND ZEROS .....	57
FIGURE A-1. EVENT FOCAL MECHANISMS.....	58
FIGURE A-2. RADIATION PATTERN VERSUS DEPTH .....	59
FIGURE A-3. RADIATION PATTERN VERSUS DEPTH .....	60
FIGURE A-4. RADIATION PATTERN AND INITIAL PHASE.....	61
FIGURE A-5. RADIATION PATTERN AND INITIAL PHASE.....	62
FIGURE B-1. STS-2 INSTRUMENT RESPONSE FROM MANUFACTURER.....	63
FIGURE B-2. STS-2 INSTRUMENT RESPONSE FROM POLES AND ZEROS .....	64
FIGURE B-3. GURALP CMG-3T302 INSTRUMENT RESPONSE .....	65
FIGURE B-4. GURALP CMG-3T INSTRUMENT RESPONSE .....	66
FIGURE B-5. GURALP CMG-3ESP AND CMG-40T INSTRUMENT RESPONSES .....	67
REFERENCES .....	68

## LIST OF TABLES

TABLE 1. SHEAR WAVE STARTING MODEL.....	31
TABLE A-1. ICEMELT EVENT PARAMETERS.....	53
TABLE A-2. HOTSPOT EVENT PARAMETERS.....	54
TABLE A-3. BORG EVENT PARAMETERS.....	55
TABLE B-1. INSTRUMENT LOCATIONS AND TYPES.....	56
TABLE B-2. INSTRUMENT POLES AND ZEROS.....	57

## LIST OF FIGURES

FIGURE 1. REYKJANES RIDGE WITH EVENTS AND STATIONS .....	32
FIGURE 2. LOVE AND RAYLEIGH WAVE GROUP VELOCITIES.....	33
FIGURE 3. RAYLEIGH WAVE ENERGY FOCUSING .....	34
FIGURE 4. LOVE WAVE ENERGY FOCUSING .....	35
FIGURE 5. PHASE VELOCITIES .....	36
FIGURE 6. ALONG AXIS VELOCITY VARIATIONS .....	37
FIGURE 7. EFFECTS OF ICELAND ON SURFACE WAVES.....	38
FIGURE 8. SHEAR WAVE VELOCITY AND ANISOTROPY .....	39
FIGURE 9. SHEAR WAVE VELOCITY UNCERTAINTIES .....	40
FIGURE 10. TEMPERATURE AND MELT .....	41
FIGURE 11. GRAVITY .....	42
FIGURE 12. PASSIVE FLOW BENEATH A MIGRATING RIDGE.....	43
FIGURE 13. MANTLE FLOW BENEATH THE REYKJANES RIDGE.....	44
FIGURE A-1. EVENT FOCAL MECHANISMS.....	58
FIGURE A-2. RADIATION PATTERN VERSUS DEPTH .....	59
FIGURE A-3. RADIATION PATTERN VERSUS DEPTH .....	60
FIGURE A-4. RADIATION PATTERN AND INITIAL PHASE.....	61
FIGURE A-5. RADIATION PATTERN AND INITIAL PHASE.....	62
FIGURE B-1. STS-2 INSTRUMENT RESPONSE FROM MANUFACTURER.....	63
FIGURE B-2. STS-2 INSTRUMENT RESPONSE FROM POLES AND ZEROS .....	64
FIGURE B-3. GURALP CMG-3T302 INSTRUMENT RESPONSE .....	65
FIGURE B-4. GURALP CMG-3T INSTRUMENT RESPONSE .....	66
FIGURE B-5. GURALP CMG-3ESP AND CMG-40T INSTRUMENT RESPONSES .....	67

## LIST OF ABBREVIATIONS

## IRIS – Incorporated Research Institutions for Seismology

IRIS is a university research consortium dedicated to exploring the Earth's interior through the collection and distribution of seismographic data. The web site is [www.iris.edu](http://www.iris.edu)

## GSN – Global Seismic Network

The global seismic network is an IRIS program that maintains seismic stations worldwide.

## EPR – East Pacific Rise

The EPR is a mid-ocean ridge in the eastern Pacific Ocean.

## SAC – Seismic Analysis Code

SAC is software package for signal processing [*Goldstein, 1996*].

## ISC – International Seismological Centre

The ISC is a non-governmental organization charged with the final collection, analysis and publication of standard earthquake information from all over the world. The web site is [www.isc.ac.uk](http://www.isc.ac.uk).

## MAR – Mid Atlantic Ridge

The MAR is a mid-ocean ridge in the central Atlantic Ocean. The Reykjanes Ridge is one section of the MAR.

## MORB – mid-ocean ridge basalt

Mid-ocean ridge basalt is the typical lava type erupted at mid-ocean ridges.

## CHAPTER 1. INTRODUCTION

Extensive volcanism at Iceland over the past 55+ million years [*Morgan*, 1981] is usually ascribed to the existence of a hot, buoyant, mantle plume [*Morgan*, 1971; *White and McKenzie*, 1989; *Wolfe et al.*, 1997; *Allen et al.*, 1999]. Likewise, along the adjacent Reykjanes and Kolbeinsey mid-ocean ridges, geochemical [e.g., *Schilling*, 1973; *Fitton et al.*, 1997; *Murton et al.*, 2002], seismic [e.g., *Smallwood et al.*, 1995; *White et al.*, 1995; *Pilidou et al.*, 2004], and seafloor morphological [e.g., *Searle et al.*, 1998] evidence for high mantle melt production is usually attributed to outward flow of plume material beneath these ridges. Although debate continues over the origin of these melt anomalies [*Foulger and Pearson*, 2001], seismic tomographic images reveal a plume-like structure in the upper mantle beneath Iceland [*Wolfe et al.*, 1997; *Foulger et al.*, 2000; *Allen et al.*, 2002; *Zhao*, 2004] and several plume-flow models have been developed to explain Icelandic volcanism and the observations along the adjacent ridges. Although the observations are most often attributed to sub-lithospheric spreading of plume material away from Iceland [*Vogt*, 1976; *Ribe et al.*, 1995; *Ito et al.*, 1996; *Ito et al.*, 1999; *Albers and Christensen*, 2001; *Ito*, 2001], the exact manner of such spreading is not yet understood.

At least two end-member models have been proposed to describe how a plume might spread outward beneath the Reykjanes and Kolbeinsey portions of the Mid-Atlantic Ridge. They are distinguished by whether the plume material is preferentially channeled down the ridge in a lithospheric channel or spreads out radially beneath the

lithosphere. In the channel flow model [Albers and Christensen, 2001], lithospheric cooling generates a rheological groove beneath the ridge via thickening of the lithosphere away from the ridge. Buoyant, low-viscosity plume material, rising in a narrow conduit beneath Iceland, is trapped and channeled within this groove. For a narrow conduit, low viscosity plume material is needed to explain the lateral extent of trace element concentrations [Schilling, 1973; Schilling, 1985] and large-scale topography and gravity anomalies [White, 1997]. In an alternate model, mantle dehydration at the onset of partial melting fills in the lithospheric groove with higher-viscosity, dehydrated plume material. Since the depth of the dehydration/high-viscosity boundary does not change significantly away from the ridge axis, lower-viscosity plume material spreads out radially beneath this boundary [Hirth and Kohlstedt, 1996; Ito et al., 1999; Ito, 2001]. Also, if the density contrast between the plume material and the ambient mantle is less than two orders of magnitude, or if the plume layer thickness is large compared to the variation in lithospheric thickness, then plume material will spread out in a radial manner [Ito et al., 2003].

This finite-frequency surface-wave tomography method was used to examine the anisotropic shear-wave structure of the upper mantle beneath the Reykjanes Ridge and to infer mantle flow, lithospheric thickness, thermal structure, and melt distribution in the mantle. These results can distinguish whether plume material flows preferentially beneath the ridge, spreads out radially, or something in between.

## CHAPTER 2. STUDY AREA

The study area encompasses the 1000-km-long Reykjanes Ridge and the 400 km section of the MAR between the Bight and Gibbs fracture zones (**Figure 1**). This is a slow-spreading ridge with full spreading rates that range from 18.5 mm/yr in the north, to 20.2 mm/yr in the south [*DeMets et al.*, 1994]. Crustal accretion is symmetric about the ridge [*Searle et al.*, 1998] even though the spreading direction is oblique to the strike of the ridge (28° from ridge normal); the ridge currently migrates southwest at ~2 cm/yr in a hotspot reference frame [*Gripp and Gordon*, 2002].

When compared to other “normal” slow-spreading ridges, the Reykjanes Ridge has many anomalous characteristics that suggest southward flow of plume material beneath the ridge. Seafloor morphology, gravity, and seismic measurements of crustal thickness provide first-order evidence for increased melt generation and associated mantle temperature or composition anomalies. For example, the average ocean depth for the MAR is ~2.5 km. However, over a distance of 1350 km the axial depth of the MAR slowly rises from 2.5 km depth, just south of the Bight Fracture Zone, to sea level on the Reykjanes Peninsula [*White et al.*, 1995]. This trend can be explained by a combination of thickening crust [*Smallwood et al.*, 1995; *Heller and Marquart*, 2002] and more buoyant material in the upper mantle [*Heller and Marquart*, 2002]. Seismic estimates of crustal thickness indicate that the crust increases from 6-7 km thick at a distance of 1500 km from central Iceland [*Whitmarsh and Calvert*, 1986], to 8-12 km under the northern Reykjanes Ridge [*Smallwood et al.*, 1995], to 38-40 km under central Iceland

[Darbyshire *et al.*, 1998]. An admittance study [Heller and Marquart, 2002] indicates that the ridge is at least partially supported by low density material in the asthenosphere.

Low lithospheric segmentation, a characteristic of the Reykjanes Ridge north of the Bight Fracture Zone, and an axial high instead of an axial valley, a characteristic of the Reykjanes Ridge north of 58°50'N, are signatures of a high melt supply [Talwani, 1971; Keeton *et al.*, 1997]. Low segmentation of the lithosphere is supported by the absence of large amplitude, segment scale, mantle Bouguer gravity anomaly variations as seen elsewhere on the MAR and nearly linear magnetic isochrons out to 10 Myr from the ridge [Searle *et al.*, 1998]. V-shaped ridges are observed in both bathymetry and gravity data that flank the ridge axis and are oriented sub-parallel to the strike of the spreading axis [e.g., Vogt, 1976; Searle *et al.*, 1998]. These ridges are thought to be caused by pulses of hot (+30°C) plume material that propagate down the ridge at a rate ten times faster than the half seafloor spreading rate [White *et al.*, 1995]. Such pulses have a primary periodicity of 5-6 Myr [Vogt, 1971; Jones *et al.*, 2002] and generate 2 km of excess crustal thickness [Vogt, 1971; White *et al.*, 1995; Ito, 2001] and a high density of seamounts [Searle *et al.*, 1998]. Periods of anomalously high melting beneath Iceland are correlated with, and may be the cause of, ridge jumps on Iceland [Jones *et al.*, 2002]. Alternatively, periods of elevated magma supply may be the result, rather than the cause, of these ridge jumps [White *et al.*, 1995; Hardarson *et al.*, 1997].

Global tomography models reveal a low velocity region in the upper mantle beneath Iceland to at least 400 km in depth and along the adjacent MAR for hundreds of kilometers [Bijwaard and Spakman, 1998; Bijwaard and Spakman, 1999; Ritsema *et al.*,

1999; Nataf, 2000; Montelli *et al.*, 2004; Zhao, 2004]. A more detailed regional surface wave study indicates an elongate low velocity zone extending beneath both Iceland and the MAR [Pilidou *et al.*, 2004] that is confined to the top 200 km of the mantle. Using seismic stations located on Iceland, shear wave splitting measurements yield anisotropy patterns that are interpreted as the result of plume material channeled outwards along the ridges [Li and Detrick, 2003; Xue and Allen, 2005]. However, to date no such observations exist on the ridges themselves to verify this interpretation. Seismic anisotropy calculated from Love and Rayleigh waves traveling along the Reykjanes Ridge suggests a vertical alignment of the crystallographic fast-axes above 100 km depth, which is interpreted as resulting from active mantle upwelling [Gaherty, 2001].

High levels of primordial volatiles and incompatible elements in Reykjanes Ridge basalts suggest a deeper and more primitive mantle source than for normal MORB. High  $^3\text{He}/^4\text{He}$  ratios [Poreda *et al.*, 1986], as compared to normal MORB, are often ascribed to a primitive mantle source, and are present along the Reykjanes Ridge to the Gibbs Fracture Zone (a distance of 1700 km). High  $^{87}\text{Sr}/^{86}\text{Sr}$  and  $^{206}\text{Pb}/^{204}\text{Pb}$ , indicators of mantle enrichment, also support hotspot influence to a distance of 1700 km south along the ridge [Taylor *et al.*, 1997]. Major and minor incompatible elements show the greatest enrichment of incompatible elements within ~800 km of the hotspot [Murton *et al.*, 2002], nevertheless Reykjanes Ridge lavas include a contribution of greater than 20% from Icelandic mantle sources at all distances from the plume center [Taylor *et al.*, 1997]. The mechanism of melt transport is not clear from these studies, but it is unlikely that melt is channeled down the ridge within the crust, because petrologic data show parent

melt diversity and a lack of connectivity between crustal magma systems [*Murton et al.*, 2002].

## CHAPTER 3. DATA

The seismic data were recorded on 38 broadband, 3-component seismometers deployed as part of the ICEMELT and HOTSPOT experiments, as well as one permanent GSN station (BORG) (**Figure 1**). The ICEMELT experiment [Bjarnason *et al.*, 1996] consisted of 15 Streckeisen STS-2 instruments, which were installed across Iceland during 1993-1995 and recorded at a rate of 10 samples per second until the autumn of 1996. The HOTSPOT experiment [Allen *et al.*, 1999] consisted of 30 Guralp CMG3-ESP, 4 Guralp CMG-40T, and 1 Guralp CMG-3T instruments, which were installed during the summer of 1996 and recorded at a rate of 20 samples per second until the summer of 1998. The BORG station contained a Streckeisen STS-2 instrument [IRIS, 2004] that recorded at 40 samples per second during the events of interest.

Fundamental mode Love (11-50s period) and Rayleigh (14-100s period) waveforms were collected from 19 earthquakes that occurred south of Iceland with event-station distances ranging from 338 km to 1863 km. After rotation of the horizontal components and correction for instrument responses, the data were narrow band-pass filtered with a Gabor filter [Yomogida and Aki, 1985] to extract discreet fundamental-mode wavelets at each center frequency. The center frequencies of the filters used for Rayleigh waves were: 0.01, 0.128, 0.02, 0.03, 0.04, 0.05, 0.053, 0.055, 0.057, 0.060, 0.065, and 0.070 Hz; for Love waves they were: 0.02, 0.03, 0.04, 0.045, 0.050, 0.055, 0.060, 0.065, 0.070, 0.075, 0.080, and 0.085 Hz. The center frequencies were more closely spaced in regions of the seismic spectrum where phase velocities changed more rapidly. The data were manually reviewed and traces with poor signal to noise ratios were

discarded. Although the data provide excellent sampling of the mantle beneath the ridge axis and outwards to the far eastern side of the ridge, there is less coverage on the far western side of the ridge since few large earthquakes occurred to the west during the recording period.

Initial examination of the data indicates lower velocities below the ridge than beneath older lithosphere. Apparent group velocities for Love and Rayleigh waves show an ~8% reduction for paths along the ridge versus paths away from the ridge (**Figure 2**). Further indication of a sub-ridge low velocity zone, amplitudes of the waveforms exhibit focusing effects. For events located on the ridge, plots of traces organized in geographic order (west to east) reveal significantly higher amplitudes for stations located near the ridge (14-33 s period for Rayleigh waves and 18-32 s for Love) (**Figure 3, Figure 4**). This focusing effect is produced by lateral refraction of surface wave energy into a low velocity zone beneath the ridge axis, which acts as a wave-guide that traps the surface wave energy [*Dunn and Forsyth, 2003*]. The patterns are somewhat different for Rayleigh versus Love waves, possibly caused by lateral variations in velocity and anisotropy; Rayleigh and Love waves would respond differently to these variations due to difference in their depth sensitivities. The amplitude focusing cannot be explained by the radiation pattern of the source, which in many cases predicts the opposite effect.

## CHAPTER 4. METHODS

The finite-frequency tomography method of *Dunn and Forsyth* [2003] solves for shear wave velocity and transverse isotropy structure. This is a two-step method that first uses the phase, group arrival time, and amplitude information of the wavelets to solve for Love and Rayleigh wave phase velocity structure, and then uses the phase velocities to solve for anisotropic shear wave velocity structure. Because the surface waves traveled roughly parallel to the ridge axis, they provided little sensitivity to along-axis variations in velocity structure. Therefore, except where otherwise noted, the solution represents an along-axis average of 2-D velocity structure of the ridge in a vertical plane oriented normal to the ridge.

In the first step, the forward problem consists of computing synthetic wavelets at the stations for a given phase velocity structure that is defined on a grid extending 1452 km across the ridge (x-axis) and 2200 km along the ridge (y-axis). Although phase velocities vary in both x and y, the y-axis variation is due simply to the bending of the ridge. Thus, at any point along the ridge, the phase velocity structure (as function of distance from the ridge and frequency) is the same. The starting model was derived from phase velocity values of the Pacific upper mantle [*Nishimura and Forsyth*, 1988] using lithospheric ages appropriate for the Reykjanes Ridge. The initial phase and radiation pattern for each event were computed from the displacement eigenfunctions and the double couple solution of the earthquake [*Aki and Richards*, 2002].

For the inverse problem, to reduce the number of parameters, the phase velocities at each period were fit to a cubic spline under tension with 15 control nodes defined at

distances of 0,  $\pm 50$ ,  $\pm 100$ ,  $\pm 175$ ,  $\pm 250$ ,  $\pm 350$ ,  $\pm 500$ , and  $\pm 726$  km from the ridge axis.

At each of these nodes, a dispersion curve was defined as a third-order (for Love waves) or fourth-order (for Rayleigh waves) polynomial. Therefore, there were 60 (Love) and 75 (Rayleigh) parameters for phase velocity. The objective of the inverse problem is to solve for the polynomial coefficients at each control node and thus determine the phase velocity as a function of frequency and distance from the ridge.

Estimates of the uncertainties of the group, phase, and amplitude information were included in the inverse problem. Uncertainties in the group arrival time were determined by the uncertainty of matching the peaks of observed and calculated waveform envelopes. The standard deviation was estimated by cross-correlating the two waveforms and taking the half-width of the primary peak at a height equal to the correlation coefficient. Using this method, oddly shaped envelopes with a low signal-to-noise ratio were assigned the greatest uncertainty. Uncertainties in amplitude were determined by the uncertainty in matching the maximum amplitudes of observed and calculated waveforms. A correlation coefficient of 1 between the envelopes of the two waveforms corresponded to a standard deviation of 20% and a correlation coefficient of 0 corresponded to a standard deviation of 60%. The minimum value of 20% was set to allow for uncertainties in the radiation pattern of the event. Uncertainties in phase were determined by the uncertainty in cross-correlating the observed and calculated waveforms. A correlation coefficient of 0.5 between the two waveforms was scaled to yield a standard deviation of one full cycle. For the few events in which no focal

mechanism was available, the initial phase was unknown so phase information was omitted.

For each event, the best available source parameters were used from the ISC [International Seismological Centre, 2001], Harvard CMT [Dziewonski *et al.*, 2004], and Engdahl [Engdahl *et al.*, 1998] catalogs. Uncertainties in the focal mechanisms, locations, and depths of the events were accounted for in the phase, group, and amplitude uncertainties. The initial phases for Rayleigh waves had negligible sensitivity to the uncertainties in event depth, but for some Love waves a depth difference of 5 km could shift the phase by  $\pi/9$  or more. However, in most cases the uncertainty was less than  $\pi/30$ , which corresponds to  $<0.01$  km/s error in phase velocity for a single 25 s wave recorded on Iceland. The combined uncertainty in the phase velocity structure due to uncertainties in the event locations (2-10 km) is  $<0.01$  km/s. Although event depth affects the absolute amplitude of Love waves, this method only requires relative amplitudes across the array. For Rayleigh waves, the depth sensitivity was only important when the event was shallow ( $<8$  km). While uncertainties in the focal mechanism could affect the relative amplitudes across the arrays, the source radiation patterns for all but the longest periods was a secondary signal to the focusing and defocusing of energy due to the sub-ridge waveguide. Amplitude uncertainties due to focal mechanism uncertainties are azimuthally dependent, but trends in the amplitudes across the seismic array are only marginally affected by this uncertainty.

It is necessary to forward model the data first, starting with the longest period waves, to ensure a proper match of the phases of calculated and observed waveforms.

Then, a joint solution for all periods and for all of the Love or Rayleigh data was accomplished via several iterations of the forward and inverse problems. The  $\chi^2$  misfit of a solution was determined from differences between the phase, amplitude, and group arrival time of the observed and calculated waveforms. Uncertainties in the phase velocity solution were estimated from a linearized error propagation approach and additional sensitivity tests, as discussed below.

In the second step, the anisotropic shear wave velocity, as a function of depth and distance from the ridge, was calculated via a joint inversion of the Love and Rayleigh wave phase velocities. Anisotropic shear wave structure was calculated in a vertical plane extending 1200 km across the ridge and 600 km in depth; density and compressional-wave velocity were also calculated as part of the inversion, although the surface waves in the period range used here have little sensitivity to these two parameters [Nishimura and Forsyth, 1988] and their solutions deviated little with respect to the starting model. The anisotropy term in the inversion is defined as  $(V_{SH}/V_{SV})^2$ , where  $V_{SH}$  is the shear wave velocity of a horizontally polarized shear wave and  $V_{SV}$  is for a vertically polarized shear wave. However, in the results presented below, the percent anisotropy is defined as  $100*(V_{SV}-V_{SH})/V_{average}$ . This type of anisotropy is often referred to as “transverse isotropy” (hexagonal symmetry with a vertical axis of symmetry) [Babuska and Cara, 1991].

The forward problem consisted of computing synthetic dispersion curves for each column of the model and then comparing them to the dispersion curves determined in step one. The starting model was made up of a 1-D depth-varying average velocity

structure for depths above 250 km and the 1-D model employed by *Gaherty* [2001] for depths below 250 km. Described in **Table 1**, each column is 10 km wide with 21 layers. Layer thickness is uniform across the model, except for the water depth [*National Geophysical Data Center*, 1993] and sediment layer [*National Geophysical Data Center*, 2005], whose thicknesses were determined by averaging known values along the ridge. Crustal thickness is not well known, so the crustal velocity model was formed from a 1-D crustal model based on Mid-Atlantic Ridge velocities [*Barclay et al.*, 2001] and a range of reasonable values for the crustal thickness (8-13 km) was tried by altering the thickness of the deepest crustal layer; a value of 11 km average total thickness resulted in the best overall fit to the data.

It is important to carefully examine any dependency that a solution may have on the starting model and constraint equations. In this case, there is the potential for trade-offs between seismic anisotropy and seismic velocity, as well as a trade-off between lithospheric and asthenospheric velocities. Thus, the result of any inversion procedure will be dependent on the relative weighting between the parameters describing those aspects of the solution. Many solutions are calculated by varying the starting model and the relative constraints on shear velocity and anisotropy. The first test examined the solution uncertainties by adding random perturbations to the starting model and the phase velocity values. Normally distributed noise was added to the Love and Rayleigh phase velocities with a standard deviation equal to the computed phase velocity uncertainties; normally distributed noise was added to the starting model with a standard deviation of 1%, or approximately 0.04 km/s. After 100 iterations, the mean and standard deviation of

those solutions that satisfy the misfit criteria were calculated, thus determining the range of viable solutions. A second test examined the trade-off between the shear velocities and anisotropy, by applying a range of *a priori* model constraints that vary the relative weighting of the two types of parameters (0.1-0.6 km/s for the shear velocity and 0.05-0.6 for the anisotropy parameters). The mean and standard deviation was calculated for those solutions that satisfy the misfit criteria. The third test examines the depth range of the low velocity zone by decreasing the *a priori* uncertainties for shear wave velocity at the bottom of the model in order to force any velocity variations to shallower depths. By examining the misfit of the data for these squeezed models, this test determined the depth constraints that the data can place on the velocity structure.

## CHAPTER 5. RESULTS

## 1. Rayleigh Wave Phase Velocity

The Rayleigh wave phase velocities (**Figure 5a**), are ~4-6% slower beneath the ridge than for lithospheric ages greater than 50 Myr, resulting in a ~500-km-wide zone of low phase velocities. Phase velocities are asymmetric about the ridge, with higher velocities to the east at shorter periods and higher velocities to the west at longer periods. Testing the significance of this asymmetry by comparing this solution to one that was generated with a symmetry requirement, an f-test indicates that at the 99% level of confidence the velocity structure is not symmetric.

Phase velocity variations along the ridge are small compared to the uncertainties of the data and solution. Solutions that allow a linear gradient in phase velocities along the ridge did not result in lower misfits. **Figure 6** contains traces from four earthquakes with event station distances of ~838-1850 km; the traces show no difference in fit with the synthetics. On the other hand, on Iceland the region around the center of the hotspot has a significant effect on seismic energy that crosses it. After correcting for the axially-invariant phase model shown in **Figure 5a**, energy crossing this region has measurable phase delays at the shorter periods as compared to energy recorded on the near-side of the region (**Figure 7**). Furthermore, stations located on the far side of Iceland that do not have event-station paths that cross the center of the hotspot record negligible delays. To remove the effect of the region around the center of the hotspot, data that cross it were not used to determine the solution shown in **Figure 5**.

A common method for computing solution variance for linear problems is described by the following equation [Tarantola, 1987],

$$C_m' = C_m - C_m G_\infty^t (G_\infty C_m G_\infty^t + C_d)^{-1} G_\infty C_m$$

where  $C_m'$  is the solution variance matrix,  $C_m$  is the initial model variance,  $C_d$  is the data covariance, and  $G_\infty$  is the final partial derivative matrix. This method may underestimate the actual solution variance for this non-linear problem, even though the character of the distribution of values is correct. Uncertainties calculated via this linearized method are then scaled based on additional sensitivity tests. Randomly perturbing the final solution and recalculating the solution misfit indicates that multiplying the linearized uncertainties by a factor of five gives a better approximation to actual uncertainties. The standard deviation for Rayleigh wave phase velocity (**Figure 5a**) is <0.05 km/s for all periods at distances between -100 to 500 km and east of -500 km for periods of 25 s and higher. To the west of -100 km at periods of less than 25 s the standard deviation is between 0.05-0.10 km/s except for the far west end of the model, where it is > 0.1 km/s for all periods.

## 2. Love Wave Phase Velocity

The Love wave phase velocities, **Figure 5b**, are ~9% slow over a ~1000-km-wide region centered beneath the ridge. Phase velocities are asymmetric about the ridge, with relatively higher velocities at distances <100 km to the west of the ridge and relatively higher velocities at distances >100 km to the east of the ridge. An f-test comparing the data misfit of symmetric and asymmetric models indicates that Love wave phase velocities are not symmetric about the ridge axis at the 99% level of confidence. Unlike

the Rayleigh wave solution, Love waves do not show a narrower low velocity zone at short periods, though there is no reason to expect similar Love and Rayleigh phase velocities, since the two wave types have different depth sensitivities and different sensitivities to anisotropy. Similar to the Rayleigh wave result, there is no detectable along axis variation in Love phase velocities. Using the same method as for Rayleigh waves to calculate the solution uncertainty, the standard deviation for Love wave phase velocities is  $<0.06$  km/s for all periods at distances between  $-100$  to  $450$  km, for all periods  $14.28$  s and above at all distances farther east of  $450$  km, and for periods  $20$  s and above for all distances east of  $-400$  km (**Figure 5b**). To the west of  $400$  km, the standard deviation exceeds  $0.06$  km/s, for all periods, to a maximum of  $0.13$  km/s at the far western end of the model.

### 3. Shear Wave Velocity and Anisotropy

From the phase velocities, we compute the shear wave velocity structure using the method of Saito [1988]. As discussed above, many solutions were computed to examine the range of models that fit the data; the average of these solutions is shown in **Figure 8**. This average shear wave velocity solution has the following characteristics: a wide and deep low-velocity zone (defined as the reduction in velocity relative to averaged values at the eastern and western edges of the model) in the upper mantle beneath the ridge (**Figure 8a**), a high-velocity lithospheric lid at the top of the mantle that grows asymmetrically in thickness with lithospheric age (**Figure 8b**), and an anisotropy pattern that indicates horizontally aligned fast-axes of anisotropy within the high-velocity

lithospheric lid and vertically aligned fast-axes near the ridge within the asthenosphere (**Figure 8c**). This sub-ridge region of vertically-aligned fast-axes of anisotropy ( $V_{SV} > V_{SH}$ ) evolves to more horizontally aligned fast-axes several hundred kilometers away from the ridge ( $V_{SH} > V_{SV}$ ). **Figure 9** shows the range of acceptable solutions (those that satisfy the data misfit criteria) as a standard deviation about the average solution of **Figure 8**.

The sub-ridge low-velocity anomaly has a maximum magnitude of ~8% at depths < 25 km near the ridge axis, up to ~6% at depths of 80 km also near the ridge axis, and as much as 2-3% to depths of ~175 km. Across the model, anomalies are consistently higher at lithospheric depths. The outer edges of the low-velocity anomaly are indistinct, but low velocities extend to at least 300 km, and perhaps as much as 500 km, from the ridge. One reason for the fading edges is that the tomographic technique seeks smooth solutions to the data. However, uncertainty in the width of the low velocity zone is also due to a trade-off between anisotropy and the isotropic shear wave velocity structure (discussed below). Even with the large uncertainty in width, in terms of lithospheric age the Reykjanes Ridge low velocity zone is 10-35 times wider than that beneath the fast-spreading East Pacific Rise (EPR), which extends out to lithospheric ages of only 1.5-3 Ma [*Dunn and Forsyth, 2003*],[*Toomey et al., 1998; Hammond and Toomey, 2003*].

Vertical squeezing tests indicate that the shear wave velocity anomaly extends to at least a depth of 140 km. Attempting to squeeze the anomaly more shallowly results in models that either do not fit the data or require unreasonably large anomalies in the crust and lithosphere. Shear wave velocity uncertainties are <0.06 km/s in the best-resolved region

of the model, between  $-200$  and  $500$  km from the ridge and above  $200$  km depth, with the lowest uncertainties in the lithosphere. Outside this region higher uncertainties exist due to poor data coverage. Models with higher isotropic shear wave velocity require less anisotropy (discussed below) and models with lower isotropic shear wave velocity require more anisotropy. Isotropic shear wave velocity is much less sensitive than anisotropy to this trade-off (**Figure 9**). In any case, both vertically aligned fast-axes and a shear wave velocity anomaly are required to be present in the upper mantle near the axis.

The shear wave velocity image reveals a high-velocity lithospheric lid at the top of the mantle that thickens asymmetrically with age, such that a thinner high-velocity lid is observed in the North American plate. A velocity of  $4.36$  km/s is used to define the bottom of the lithosphere in order to compare these results to the model from *Zhang and Lay* [1999]. However, using a different velocity would result in different values for the thickness of the lithosphere. Using this value, the lithosphere is  $\sim 20$  km thick near the ridge axis,  $\sim 55$  km thick at a distance of  $300$  km from the ridge in the Eurasian plate, but only  $\sim 30$  km thick at a distance of  $300$  km from the ridge in the North American plate. In the Eurasian plate, these results are in agreement with the lithospheric thickness model of *Zhang and Lay* [1999]. Using the same reference velocity for the base of the lithosphere, their model predicts that lithospheric thickness ranges from  $20.4$  km at the ridge, to  $60.4$  km at  $\sim 300$  km from the ridge.

Anisotropy exists in the asthenosphere such that vertically polarized shear waves travel up to  $4.5\%$  faster than the average between  $0$  and  $200$  km east of the ridge and up

to 1.5% faster than average between 0 and 200 km west of the ridge. In both cases measurable anisotropy is limited to the upper ~150 km of the mantle or less. In the lithosphere, horizontally polarized shear waves are slightly faster than vertically polarized shear waves near the ridge axis, increasing in magnitude with distance from the ridge. Uncertainties in anisotropy are <0.5% in all regions of the model except in the lithosphere at the far eastern and western ends of the model, where it is much larger due to loss of resolution. Results for the asthenosphere agree with *Gaherty* [2001], except that these higher-resolution results reveal an asymmetry in anisotropy across the ridge, with greater anisotropy to the east, and an additional  $V_{SH} > V_{SV}$  pattern at lithospheric depths; we also do not see  $V_{SH} > V_{SV}$  below 100 km in depth.

## CHAPTER 6. INTERPRETATION

In terms of temperature only, the shear wave velocity anomaly can be explained by lateral temperature variations of up to 400°C at shallow mantle depths and 250°C at depths of 50-160 km using the attenuation model of *Gaherty* [2001] and the temperature derivative with respect to shear wave velocity determined by *Karato* [1993] (**Figure 10**). In the uppermost mantle, lateral variations of 400°C are entirely reasonable, because it simply reflects the cooling and thickening of the lithosphere with age and distance from the ridge axis. On the other hand, the lateral variations calculated for greater depths exceed estimates based on a geochemical study, which predict variations of <100°C in the upwelling zone [*White et al.*, 1995]. Excess temperatures calculated by highlighting the sensitivity of shear wave velocity to temperature, attenuation, and grain size also indicate that excess temperatures are <100°C [*Faul, pers. comm.*, 2006, *Faul and Jackson*, 2005]. Taking 100°C as the maximum temperature variation possible at these depths, then the remaining portion of the seismic anomaly can be explained by up to 0.7% partial melt (assuming relaxed moduli and assuming that melt is organized in tubules at fractions less than 1% [*Hammond and Humphreys*, 2000])

One way to narrow the range of acceptable temperature and melt fraction models is to compare gravity data collected across the Reykjanes Ridge with synthetic gravity values calculated for our seismically-derived models of thermal structure and melt distribution. Satellite gravity data [*National Geophysical Data Center*, 1993] were collected between the Reykjanes Peninsula and the Bight Fracture Zone. These data were corrected for the effect of the water and sediment layers, and for a uniform thickness

crust; the values were averaged along the ridge to produce a 1200 km wide profile that is centered on the ridge. Gravity values are  $\sim 120$  mGal lower at the ridge than at distances  $>400$  km to the west, and  $\sim 170$  mGal lower at the ridge than at distances  $>400$  km to the east. Density anomalies are calculated from the temperature and melt fraction models using a coefficient of thermal expansion that ranges from  $3.5e-5 \text{ K}^{-1}$  in the lithosphere to  $2.0e-5 \text{ K}^{-1}$  at the transition zone, and by replacing the appropriate percentage of solid mantle with melt and calculating the density of the composite ( $3300 \text{ kg/m}^3$  for solid mantle,  $3000 \text{ kg/m}^3$  for melt). The two-dimensional method of *Talwani* [1959] was used to compute the synthetic gravity anomaly.

The presence of  $<1\%$  partial melt has little effect on the overall gravity signal. If the gravity anomaly is calculated assuming that the entire shear wave velocity anomaly is due to melt, gravity is reduced by only  $\sim 5$  mGals at the ridge axis versus distances  $>400$  km away, because the predicted melt fraction is a maximum of 1% and melt is only 6-10% less dense than solid mantle. On the other hand, gravity is reduced by up to  $\sim 120$  mGal when assuming that the velocity anomaly is caused only by elevated temperatures (**Figure 11**). Though gravity suggests a slightly narrower anomaly, a model with a  $400^\circ\text{C}$  thermal anomaly at lithospheric depths (due to thin axial lithosphere versus thick lithosphere away from the ridge) with a sub-lithospheric temperature anomaly of  $100\text{-}250^\circ$  in the depth range of  $\sim 50\text{-}175$  km agrees very well with both the seismic velocity structure and the gravity data, but not with models based on the geochemical data. However, temperatures predicted from geochemistry are highly dependent on the melting model and starting composition. The asymmetry in the gravity data across the ridge can

be accounted for by temperatures that are slightly higher to the west of the ridge than to the east, as indicated by the seismic results. At the eastern and western edges, the synthetics do not match the effects of the continental margins, which are seen in the satellite data as downward trends. The synthetics also do not match an additional narrow  $\sim 30$  mGal gravity low at the ridge axis, which arises from some feature too narrow or shallow to be modeled by the existing seismic data. This feature could simply be an additional thinning of the lithosphere at the ridge axis that is not resolvable with the seismic data, or it could be a shallow and narrow region of melt in the uppermost mantle and crust. Most likely it is both.

Anisotropy in the upper mantle is typically attributed to the alignment of the fast (a-axes) of olivine crystals due to shear deformation as a result of differential mantle flow such that the a-axes aligns in the direction of mantle flow [Hess, 1964]. The patterns of  $V_{SH} > V_{SV}$  at lithospheric depths and  $V_{SV} > V_{SH}$  at greater depths found in this study may simply be the result of horizontal mantle flow at shallow depths as the plates spread apart versus vertical upward flow at greater depths. Gaherty [2001] and Braun, *et. al.*, [2000] have suggested that the  $V_{SV} > V_{SH}$  form of anisotropy is due to buoyant upwelling. In general, it is important to note that Love-Rayleigh wave anisotropy does not indicate the orientation of the fast-axes of crystals. Instead, it only suggests whether the fast-axes are predominantly vertically aligned, versus predominantly horizontally aligned.

Across the ridge, the asymmetry in the deeper pattern may be related to asymmetric mantle flow due to asymmetric plate divergence (**Figure 8c**). In the spreading direction, the Eurasian plate is nearly stationary (5.9 mm/yr westward) with

respect to the mantle and the North American plate is moving  $\sim 25.4$  mm/yr westward [Gripp and Gordon, 2002](**Figure 12**). In the upper mantle beneath the Eurasian plate, the strong positive anisotropy ( $V_{SV} > V_{SH}$ ) could be due to vertical shear with a near absence of horizontal shear between the lithosphere and asthenosphere. Beneath the North American plate, the weaker  $V_{SV} > V_{SH}$  signal is then due to a component of horizontal shear induced by the overriding plate. In general, with distance from the ridge, an increasing  $V_{SH} > V_{SV}$  at all depths is possibly due to the cumulative affect of horizontal shear.

If asymmetry in the thickness of the lithosphere is a real feature, it suggests that the American plate cools more slowly than the Eurasian plate. A more shallow average bathymetry ( $\sim 600$ m) to the west of the ridge also suggests a slower cooling rate for the North American plate. However, there is no evidence in the tomography that the entire upper mantle is hotter beneath the North American plate. Alternatively, this asymmetry could be the result of preferential sampling by the surface wave ray paths. With increasing distance from the ridge to the west, sampling is increasingly biased towards the region closer to Iceland. However, the asymmetry can be seen very close to the ridge where there is no sampling bias.

## CHAPTER 7. DISCUSSION

The Icelandic hotspot has been coincident with the North Atlantic Ocean for at least 40 Ma [Lawver and Muller, 1994] and coincident with the Reykjanes Ridge for the last 16 Ma [White, 1997]. This study shows that a significant part of the upper mantle in the North Atlantic is affected by the Icelandic hotspot (**Figure 13**). The low velocity zone, at ~700 km width, fills at least half of the distance between the continental shelf of Greenland and the Rockall Plateau, a continental block to the northwest of Ireland. This low velocity zone indicates elevated temperatures, the presence of partial melt, or both within this region. Though this study examines the upper mantle up to distances of 600 km from the ridge, there may be compositional effects at these or greater distances that cannot be imaged with seismic tomography. If active off-axis volcanism exists, the geochemical analysis of such locations could confirm the lateral extent of plume influence; no such studies are known to exist. Even though the tomographic image represents an along axis average structure, there is independent evidence from geochemistry [Taylor et al., 1997; Murton et al., 2002] that the upwelling region between Iceland and at least the Bight Fracture zone is contaminated with material from Iceland, and independent evidence from seismology [Pilidou et al., 2004] that most of the upper mantle between Iceland and at least the Bight Fracture Zone has anomalously slow shear wave velocities.

These results show that plume material from beneath Iceland is not confined to a rheological groove formed by the cooling of the lithosphere. Anomalously slow material is seen in the upper mantle beneath lithospheric ages of 0 to ~35 Ma, over which the

lithosphere is observed to thicken by 10-25 km, and to depths at least 100 km deeper than the bottom of the lithosphere. If such a groove exists, it is either filled by high viscosity material due to the dehydration of the mantle [*Hirth and Kohlstedt, 1996; Ito et al., 1999*], or the layer of spreading plume material beneath the lithosphere is voluminous enough to fill this groove and also spread out in a broader manner at greater depths.

Vertically polarized shear waves are observed to be faster than horizontally polarized shear waves in the upper mantle within 200 km of the ridge, indicative of vertical flow. Buoyancy-driven flow, although not required by this study, is inferred from along-axis flow [*White et al., 1995*], and could enhance the development of vertically aligned olivine fast-axes in the upwelling zone [*Gaherty, 2001*]. This region, where  $V_{SV} > V_{SH}$ , is asymmetric across the ridge with greater differences between  $V_{SV}$  and  $V_{SH}$  beneath the Eurasian plate. Models of passive mantle flow, due to plate spreading and ridge migration, predict the mantle is nearly stagnant beneath the Eurasian plate in the spreading direction leading to a near absence of corner flow to the east (**Figure 12**). Though buoyancy-driven upwelling could generate corner flow to the east, if there is a shallow, dehydrated, and high-viscosity plume layer [*Ito et al., 1999*], then passive, plate-driven flow will dominate in the upper 100 km. If olivine fast-axes develop a more vertical alignment during upwelling beneath the ridge, this fabric will be preserved beneath the Eurasian plate due to the lack of horizontal strain. The  $V_{SV} > V_{SH}$  region beneath the North American plate could also be caused by the development of a more vertical alignment of olivine fast-axes in a broad upwelling zone. Since there is horizontal shear beneath this plate, the alignment of fast-axes is expected to favor a

horizontal orientation with increasing lithospheric age, though this transition is not instantaneous [*Kaminski and Ribe, 2002*]. A similar phenomenon is seen in the Pacific where  $V_{SV} \approx V_{SH}$  at the ridge, but  $V_{SH}$  becomes increasing fast compared to  $V_{SV}$  with increasing lithospheric age [*Nishimura and Forsyth, 1988*]. Though a pattern in which  $V_{SV} > V_{SH}$  is not observed near the ridge, the development of increasing  $V_{SH}$ , presumably due to the presence of horizontal shear, is observed.

These results show that the thickness of the lithosphere is asymmetric across the ridge with a greater thickness in the Eurasian plate (**Figure 8b**). This is consistent with gravity data as described above and suggests that the lithosphere of the North American plate cools more slowly than that of the Eurasian plate. This could be caused by asymmetric accretion, although accretion is symmetric at the Reykjanes Ridge. It could also be caused by ridge migration. However, at the faster spreading EPR, *Toomey et al., [2002]* conclude that neither asymmetric accretion, nor ridge migration is sufficient to explain observed asymmetry in gravity, seismic velocities, and bathymetry [*Canales et al., 1998; Scheirer et al., 1998; Toomey et al., 1998; Webb and Forsyth, 1998*] using models that have passive upwelling and no heterogeneities in the mantle. They suggest that hot material from the Pacific superswell region flows to the EPR and causes the observed asymmetries. Beneath the Reykjanes Ridge, if material from Iceland is preferentially directed beneath the North American plate, it may explain observed asymmetry in the thickness of the lithosphere. The modeling of *Yale and Phipps Morgan [1998]* indicates that mantle flow in the asthenosphere in the North Atlantic is preferentially directed toward the west due to the recession of the North American

continental margin. As the continental root migrates westward, a zone of negative pressure develops behind the root in the upper mantle drawing in material from adjacent regions. To the east, the Eurasian plate does not appreciably recess from the Reykjanes Ridge and so there is no such effect.

## CHAPTER 8. CONCLUSION

The along axis average of shear wave velocity and anisotropy is calculated for the upper mantle beneath the Reykjanes Ridge as a function of depth and distance from the ridge using Love and Rayleigh waves generated by earthquakes south of Iceland and recorded by stations on Iceland. Shear wave velocity and transverse isotropy constrains the thermal properties, presence of melt, and nature of mantle flow beneath the Reykjanes Ridge. There is a low velocity zone in the upper mantle that is broad and deep relative to observations at the EPR and is consistent with elevated temperatures (up to 400°C at lithospheric depths and 250°C at greater depths), a small amount of partial melt (<0.8%), or some combination of both. Gravity observations and modeling are consistent with elevated temperatures in the mantle. The observed along-axis average shear wave velocity anomaly indicates that low velocities that persist to a depth of at least 140 km, a width of at least 600 km, and perhaps up to 1000 km across ridge cannot be explained by decompression melting alone at this slow-spreading ridge, and that plume material is too viscous to be strongly channeled along the ridge. There is shear wave anisotropy such that vertically polarized waves are faster than horizontally polarized waves throughout the uppermost mantle within ~200 km of the ridge axis, with greater differences between  $V_{SV}$  and  $V_{SH}$  to the east of the ridge. Anisotropy could be explained by passive mantle flow in the upper 100 km of the mantle where the vertical alignment of the fast-axes of olivine, developed in the upwelling zone, is preserved beneath the Eurasian plate because of the lower horizontal shear. Beneath the North American plate, the alignment of olivine fast-axes developed during upwelling is altered by horizontal shear. Buoyant

flow may also be a factor in the development of vertically aligned olivine fast-axes.

There is asymmetric thickening of the lithosphere with greater thickening on the Eurasian plate that may be due to a higher flux of hot mantle beneath the North American plate.

This is supported by gravity data and may be the result of the continental margin of North America receding from the ridge, drawing upper mantle flow in its wake.

TABLE 1. SHEAR WAVE STARTING MODEL

Table 1. Starting model for the shear wave velocity inversion. Not shown are the thicknesses of the water and sediment layers, which vary across the model and are retrieved from the National Geophysical Data Center.

Layer Thickness (km)	Depth (km)	Vp (km/s)	Vs (km/s)	Density (kg/m <sup>3</sup> )
<Water Layer>	<Water Layer>	1.5008	0	1.04
<Sediment Layer>	<Sediment Layer>	2.0973	1.8922	1.5
3	3	5.106	3.262	2.6
3	6	6.0899	3.5902	2.8
5	11	6.2799	3.7047	3
3	14	8.2635	4.8837	3.3
4	18	8.2471	4.8811	3.3
5	23	8.1358	4.7675	3.3
6	29	7.8279	4.5161	3.34
8	37	7.8202	4.4625	3.345
10	47	7.8137	4.42	3.351
15	62	7.8094	4.3408	3.361
25	87	7.8078	4.27	3.371
50	137	7.9084	4.2367	3.372
50	187	8.0061	4.2682	3.402
50	237	8.1015	4.3718	3.439
50	287	8.2003	4.4821	3.472
50	337	8.4001	4.5806	3.501
50	387	8.6	4.6802	3.515
50	437	9.2	4.8701	3.68
100	537	9.6	5.14	3.82

FIGURE 1. REYKJANES RIDGE WITH EVENTS AND STATIONS

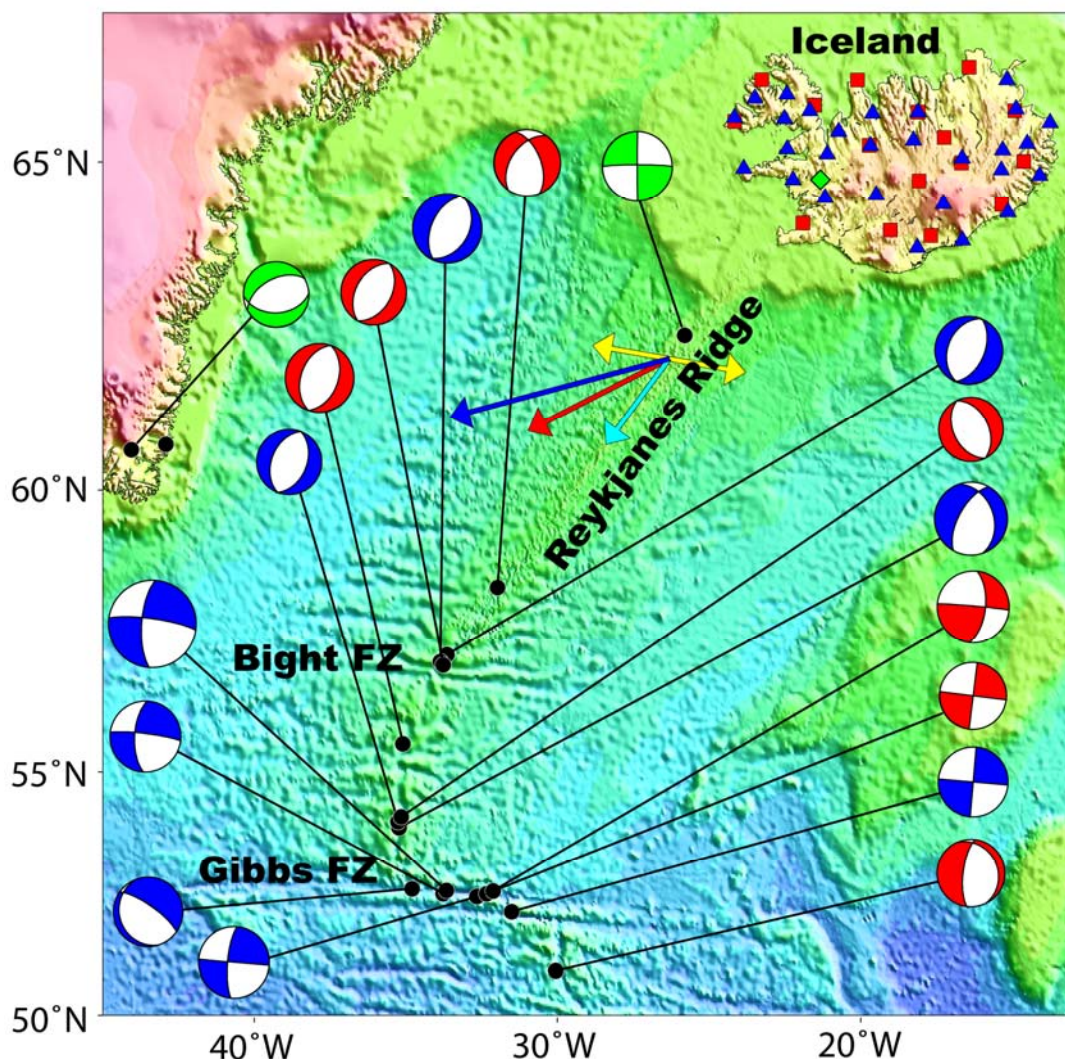


Figure 1. Satellite predicted bathymetry map of the Reykjanes Ridge showing the location of the ICEMELT array (red squares), the HOTSPOT array (blue triangles), and the BORG station of the Global Seismograph Network (green diamond). Also shown are the locations and focal mechanisms of earthquakes used in this study. The colors of the focal mechanisms correspond with the array that recorded the earthquakes with the exception of the BORG station, which recorded all earthquakes shown. The yellow vectors indicate the relative spreading of the North American plate and the Eurasian plate. The dark and light blue vectors indicate the absolute motion of the North American and Eurasian plates, respectively, in the hotspot reference frame. The red vector indicates the absolute motion of the plate boundary in a hotspot reference frame.

FIGURE 2. LOVE AND RAYLEIGH WAVE GROUP VELOCITIES

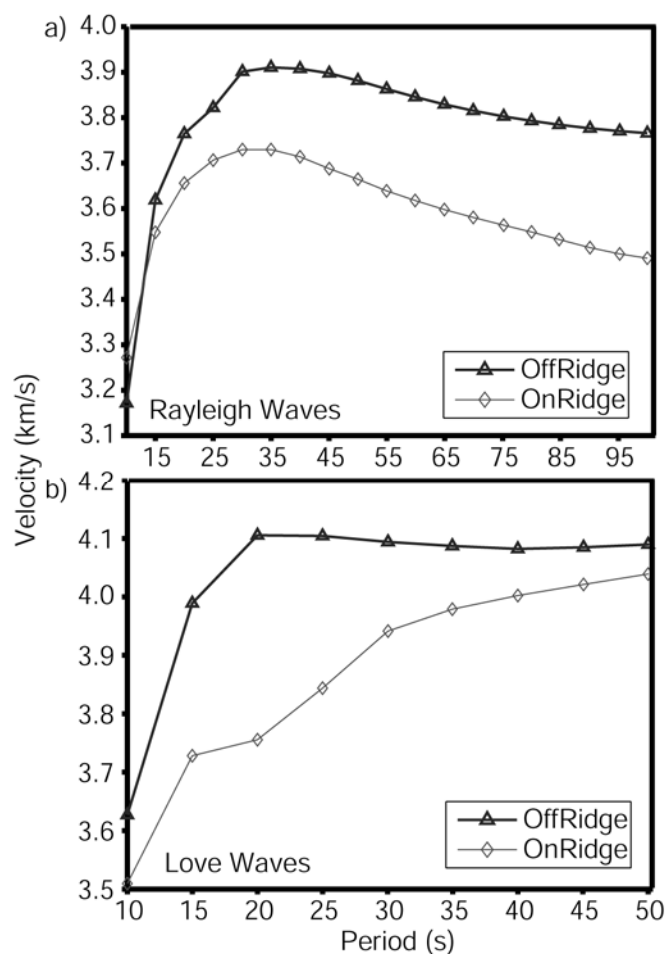


Figure 2. Average apparent Rayleigh (a) and Love (b) wave group velocity, for ray paths that traveled both near and far from the ridge axis, demonstrate slower velocities near the ridge axis. Apparent group velocity is calculated by dividing the event-station distance by the arrival time of the highest amplitude in the Love and Rayleigh narrow-band wavelet. For on-axis ray paths, events located on the Reykjanes Ridge are paired with stations located near the ridge axis. For off-axis ray paths, events located furthest away from the Reykjanes Ridge on the Gibbs Fracture Zone are paired with stations located in the far eastern part of Iceland. Data for rays that sample both on and off-axis regions are not included in this figure.

FIGURE 3. RAYLEIGH WAVE ENERGY FOCUSING

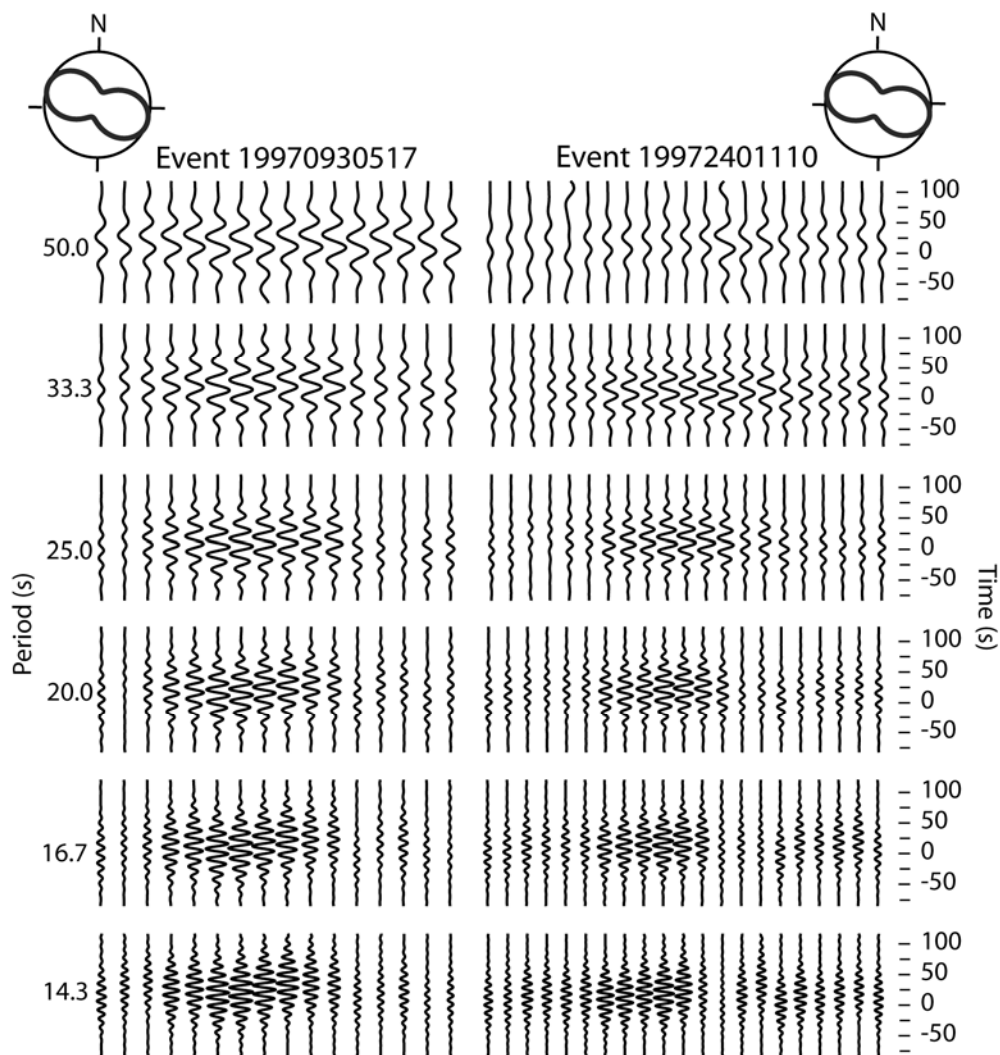


Figure 3. Rayleigh wave traces for two representative on-axis earthquakes (left and right columns) show amplitude focusing for energy traveling along the Reykjanes Ridge. The event-station distance is  $\sim 1000$  km for event 19970930517 and  $\sim 1400$  km for event 19972401110. The timing of the traces are corrected for distance and shown in geographic order from west to east. A low velocity region beneath the ridge acts as a wave-guide and traps the energy of the Rayleigh waves. Wave focusing increases with decreasing period because waves at lower periods are more sensitive to lateral variations in the phase velocity until, at the lowest periods, the amplitude pattern becomes more chaotic due to increased scattering. This wave focusing cannot be accounted for by the radiation pattern of the source mechanisms, shown at the upper left and right of each column.

FIGURE 4. LOVE WAVE ENERGY FOCUSING

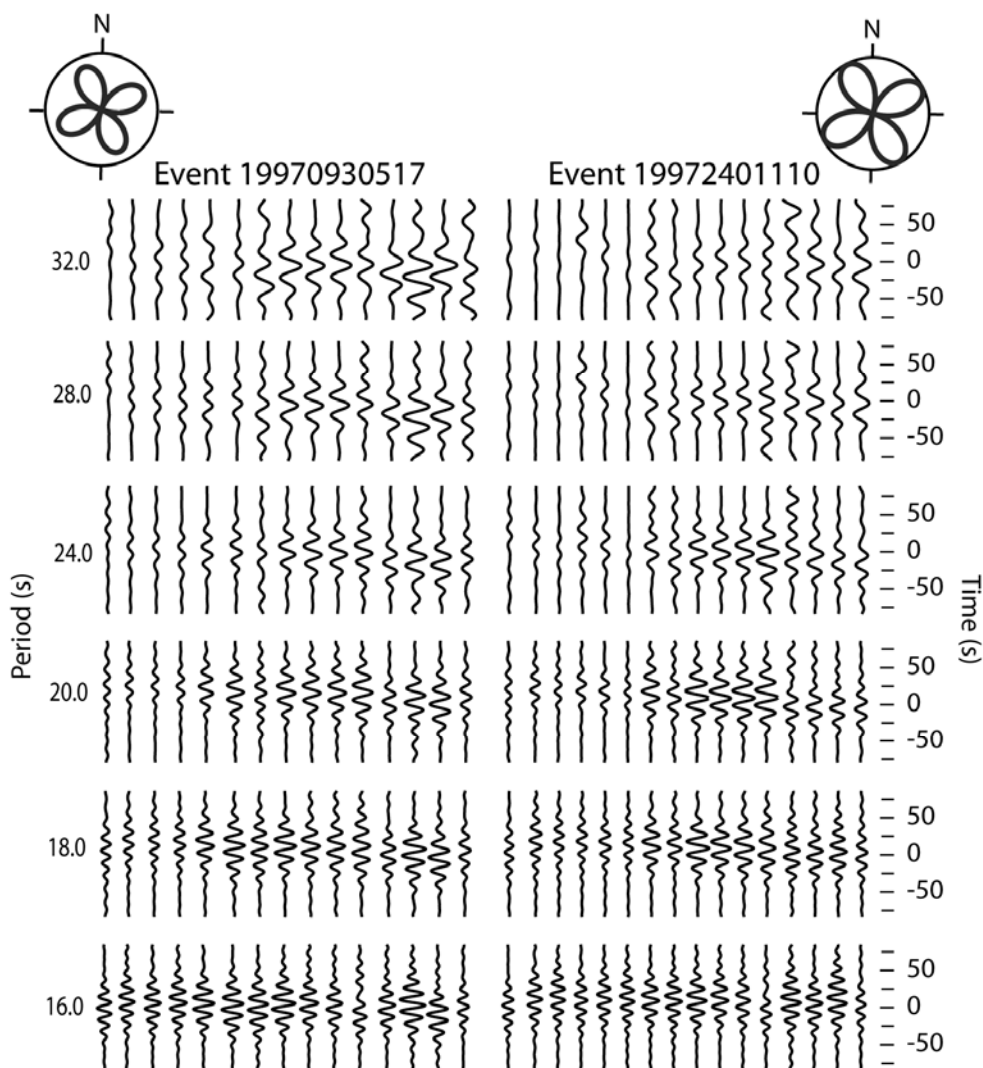


Figure 4. Love wave traces for two representative on-axis earthquakes (left and right columns) show amplitude focusing for waves traveling along the Reykjanes Ridge. The focusing effect is less for Love waves than it is for Rayleigh waves (Figure 3). The maximum focusing is seen for periods of 18-24 s. The source radiation patterns for the two earthquakes are shown in the upper left and right of each column.

FIGURE 5. PHASE VELOCITIES

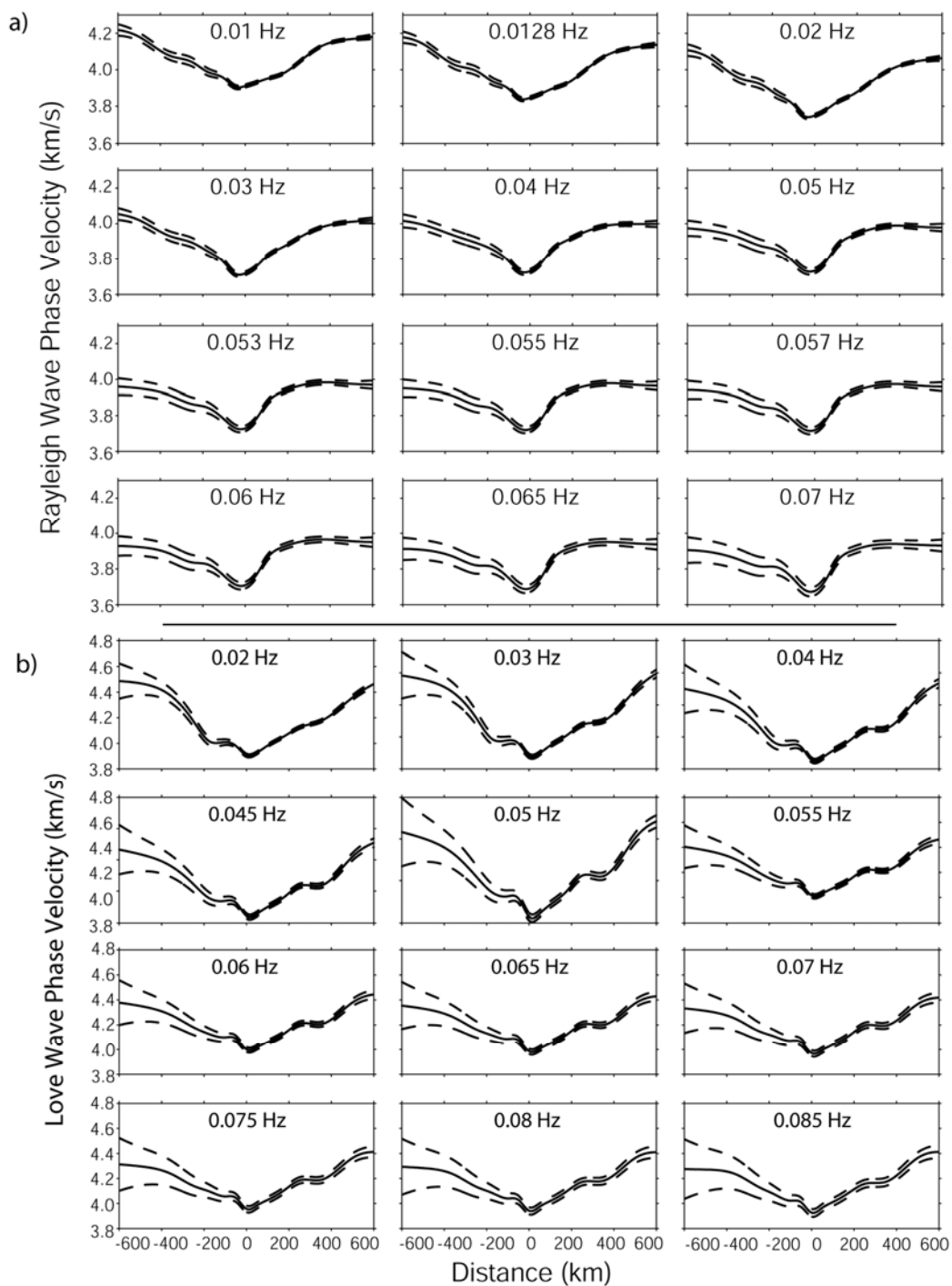


Figure 5. Plots show the Rayleigh (a) and Love (b) phase velocity solutions (solid curves), along with standard deviations (dashed curves); as a function of frequency. The horizontal axis represents distance from the ridge axis.

FIGURE 6. ALONG AXIS VELOCITY VARIATIONS

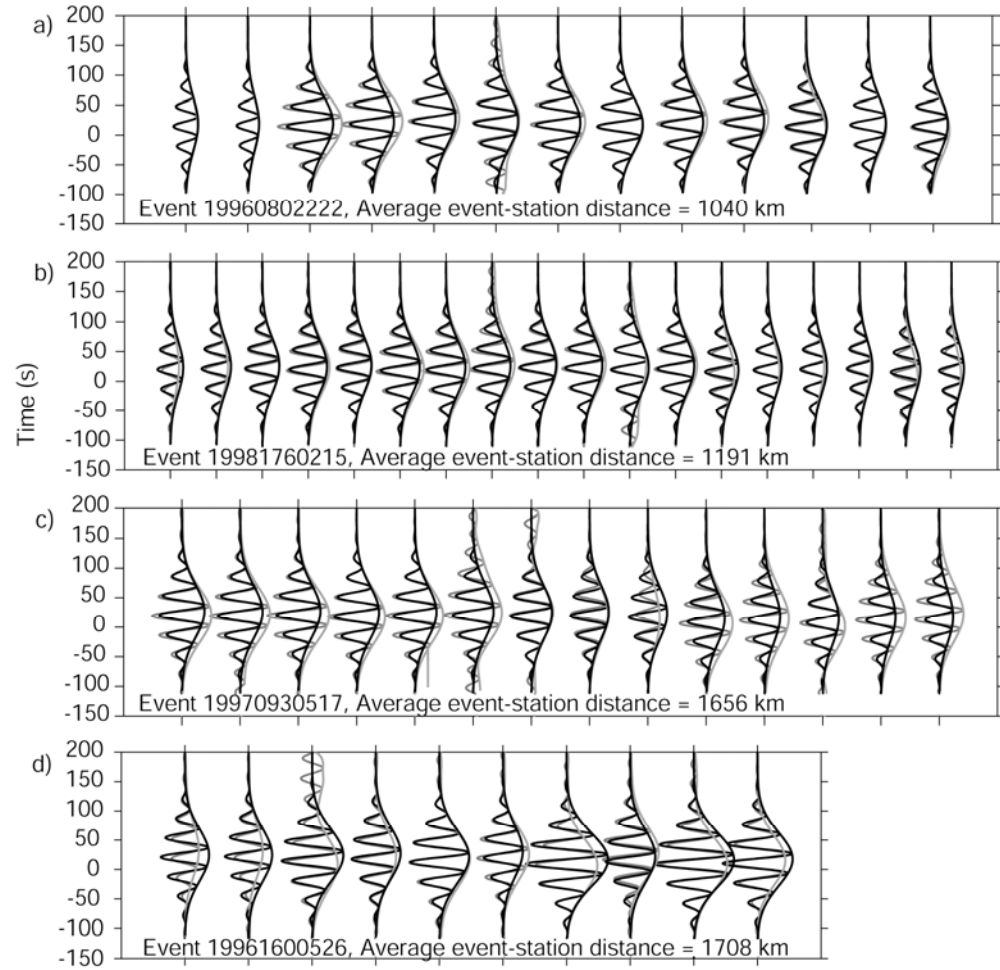


Figure 6. Plots show Rayleigh waveforms for four events at different distances from Iceland. This figure shows that the model fit does not depend on event-station distance. The average event to station distances for events shown are: a) 1040 km, b) 1191 km, c) 1656 km d) 1708 km, yet the model fit is the same for each of these events. Since the event-station distance does not affect the misfit for a modified 1D model, the along-axis variations in phase velocity are too small to be detected by this experiment.

FIGURE 7. EFFECTS OF ICELAND ON SURFACE WAVES

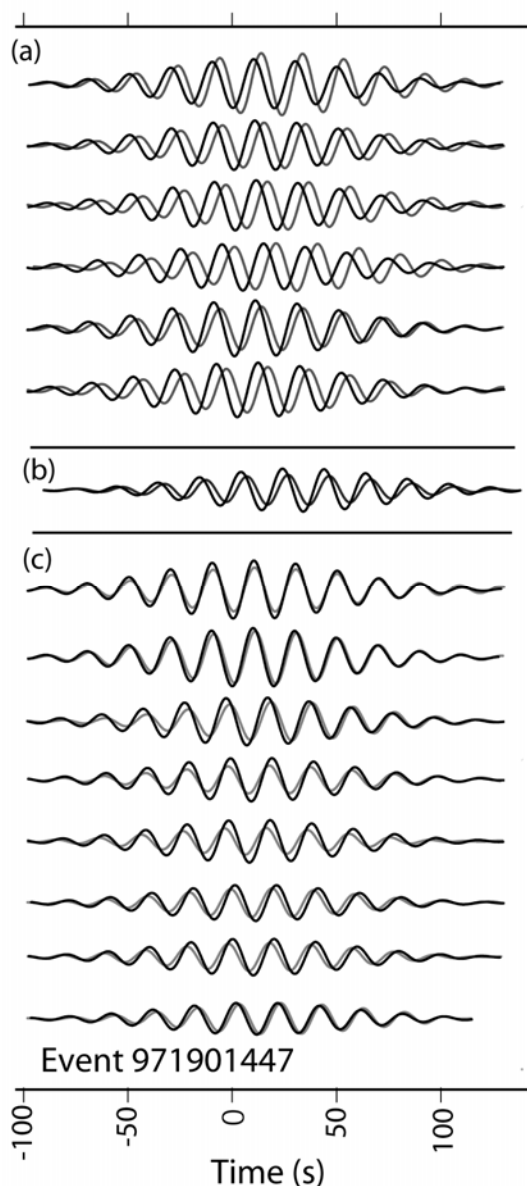


Figure 7. Plot shows traces for event 971901447 for Rayleigh waves at a period of 20s. This figure shows the effect of the region surrounding the center of the Icelandic hotspot on surface wave phase velocities. Traces from stations that are behind the center of the hotspot (a) are delayed compared to the synthetic traces generated from the best fitting along axis average phase velocity model. A trace near the back of Iceland but not behind the center of the hotspot shows only a slight delay (b). Traces for representative stations that are located near the front of Iceland, between the event and central Iceland (c) show no delay. The region surrounding the center of the hotspot has a significant effect on the phase velocity of surfaces waves.

FIGURE 8. SHEAR WAVE VELOCITY AND ANISOTROPY

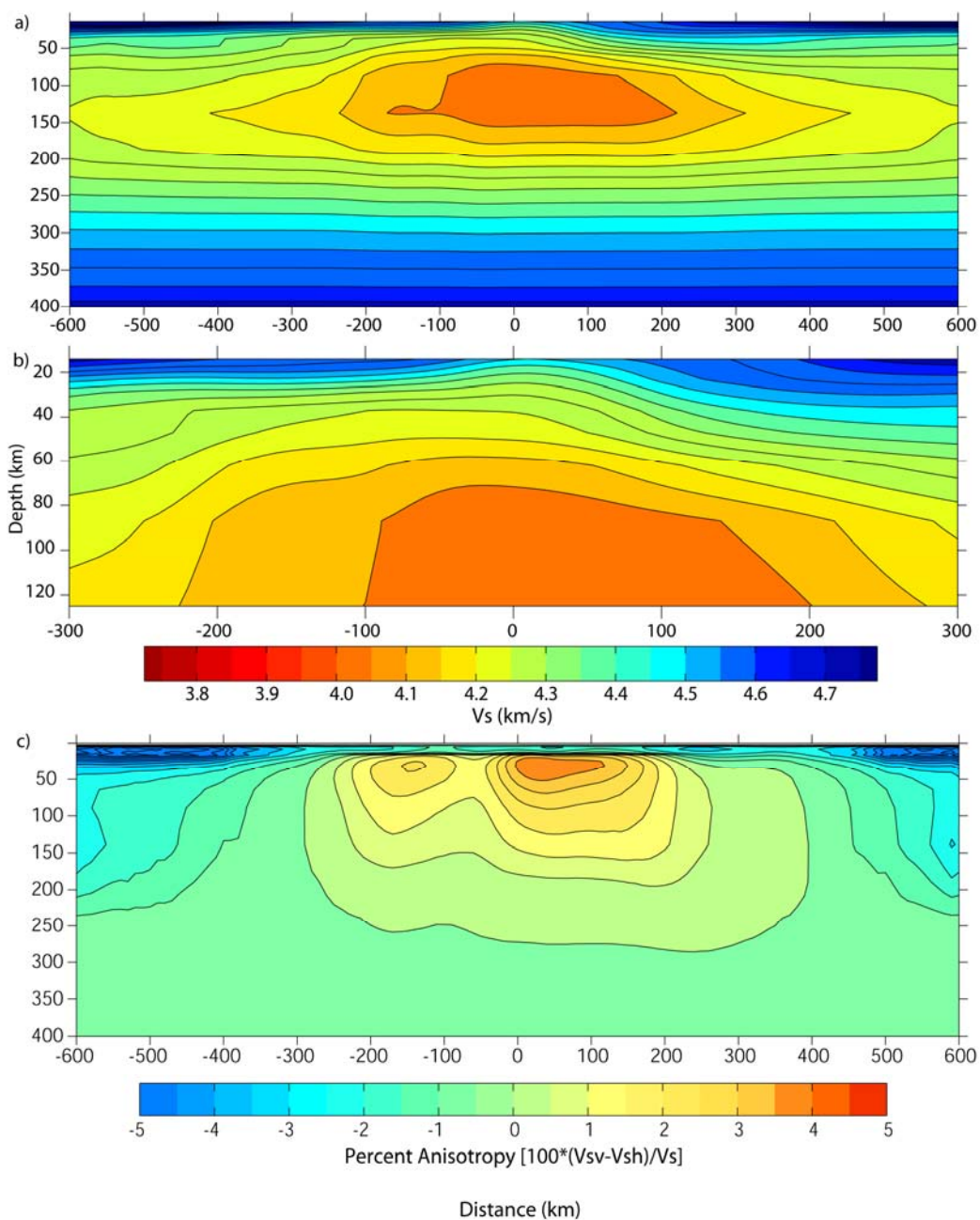


Figure 8. (a) Shear wave velocity calculated from joint inversions of Love and Rayleigh wave data. (b) A close-up of the shear wave velocity structure near the ridge axis. (c) The distribution of seismic anisotropy. The magnitude of transverse isotropy, defined as  $100 \cdot (V_{sv} - V_{sh}) / V_s$ , is shown in (c). In all plots, the horizontal axis indicates distance from the ridge axis and the vertical axis indicates depth. All values are along axis averages.

FIGURE 9. SHEAR WAVE VELOCITY UNCERTAINTIES

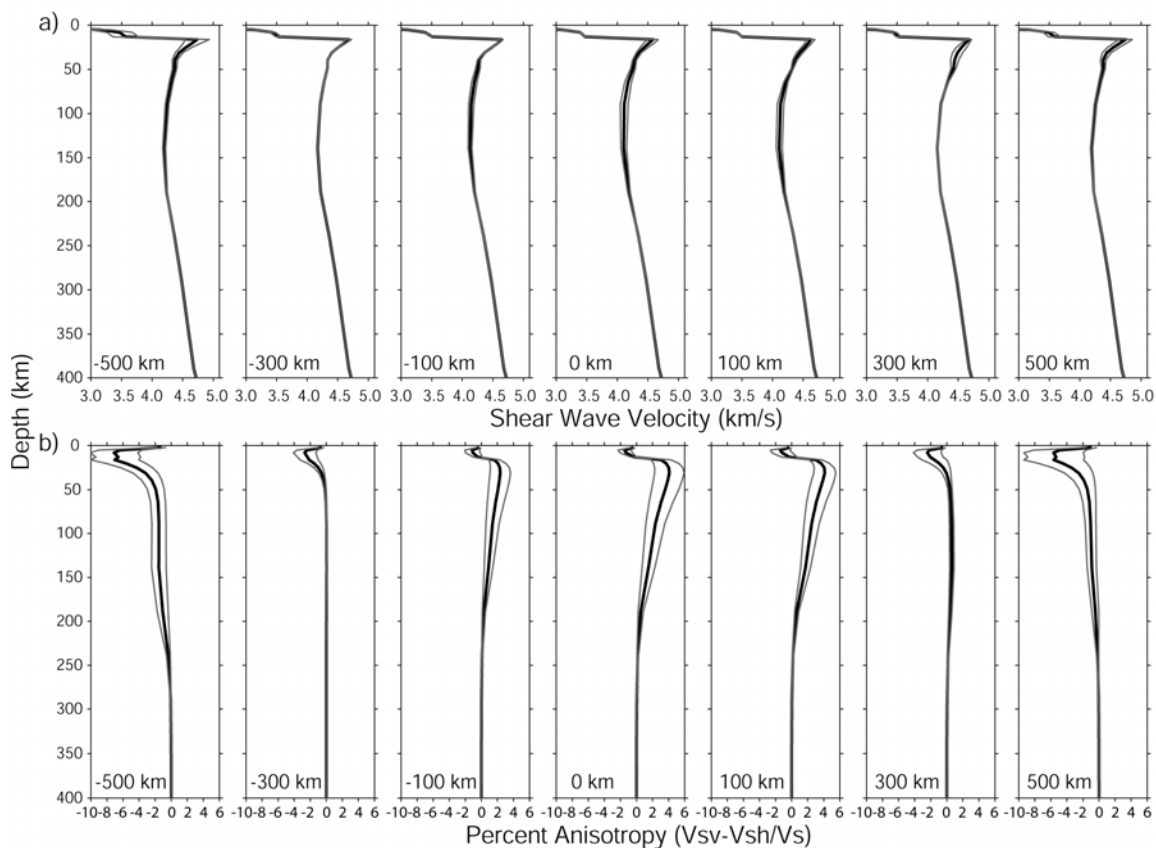


Figure 9. (a) Shear wave velocity and (b) transverse isotropy as a function of depth. The distance each profile is from the ridge axis is indicated on each plot. Error bars indicate one sigma uncertainties. Though there is more uncertainty in anisotropy than in shear wave velocity,  $V_{sv} > V_{sh}$ , is a robust feature of the upper mantle. There is a thick, fast lithosphere above a deep low velocity zone in the upper mantle.

FIGURE 10. TEMPERATURE AND MELT

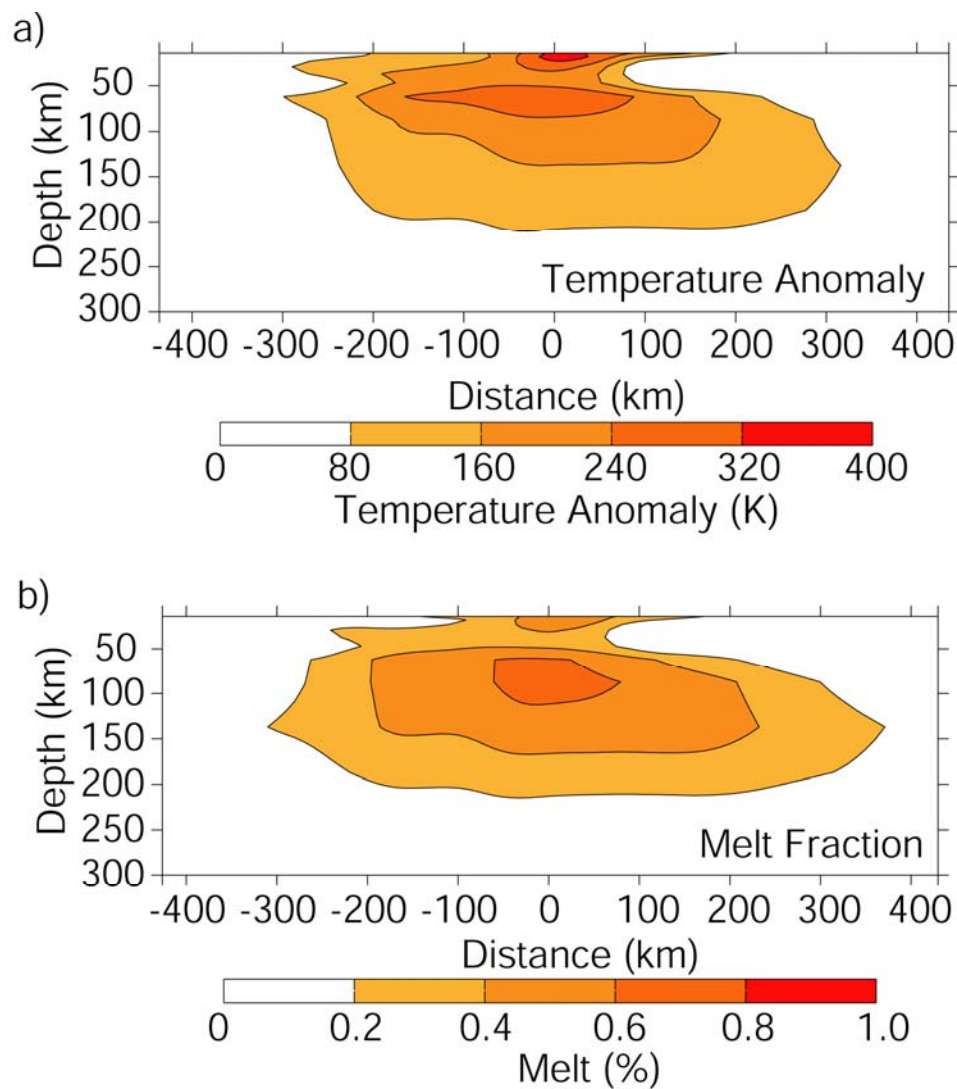


Figure 10. Shown is (a) the temperature anomaly required if the shear wave anomaly is due entirely to elevated temperatures [Karato, 1993] and (b) the distribution of partial melt if the shear wave anomaly is due entirely to partial melt [Hammond and Humphreys, 2000].

FIGURE 11. GRAVITY

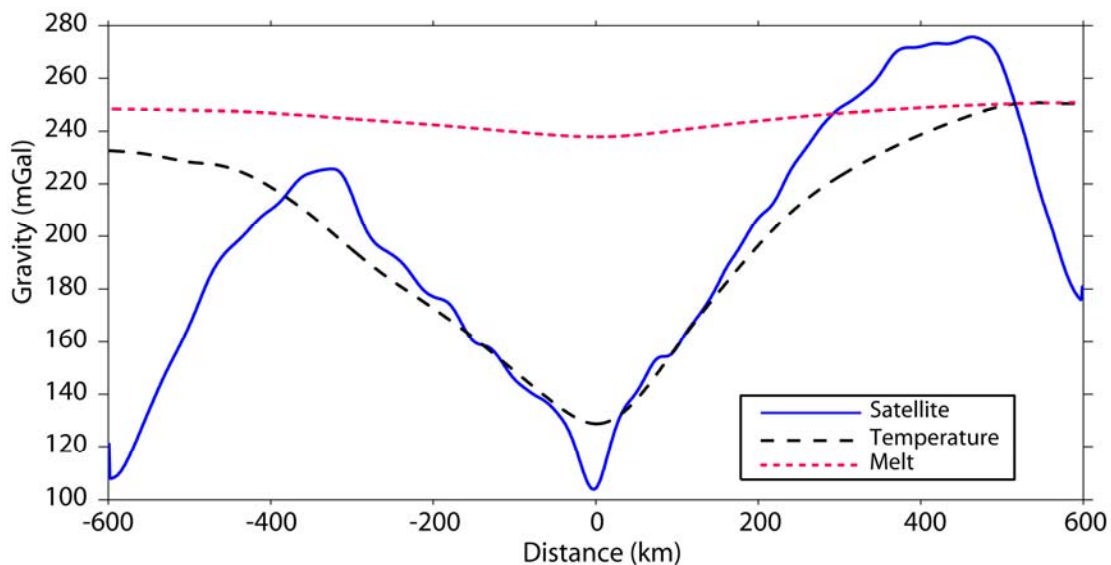


Figure 11. Shown are the along-axis average gravity profiles of the Reykjanes Ridge determined from satellite data and calculated from shear wave velocities. Gravity from shear wave velocities was calculated by first converting the shear wave velocity anomaly to a temperature anomaly and by converting the shear wave velocity anomaly to a melt anomaly, and then converting the temperature and melt anomalies to a density anomaly. Interpreting the shear wave anomaly as a temperature anomaly is more consistent with the satellite-derived data.

FIGURE 12. PASSIVE FLOW BENEATH A MIGRATING RIDGE

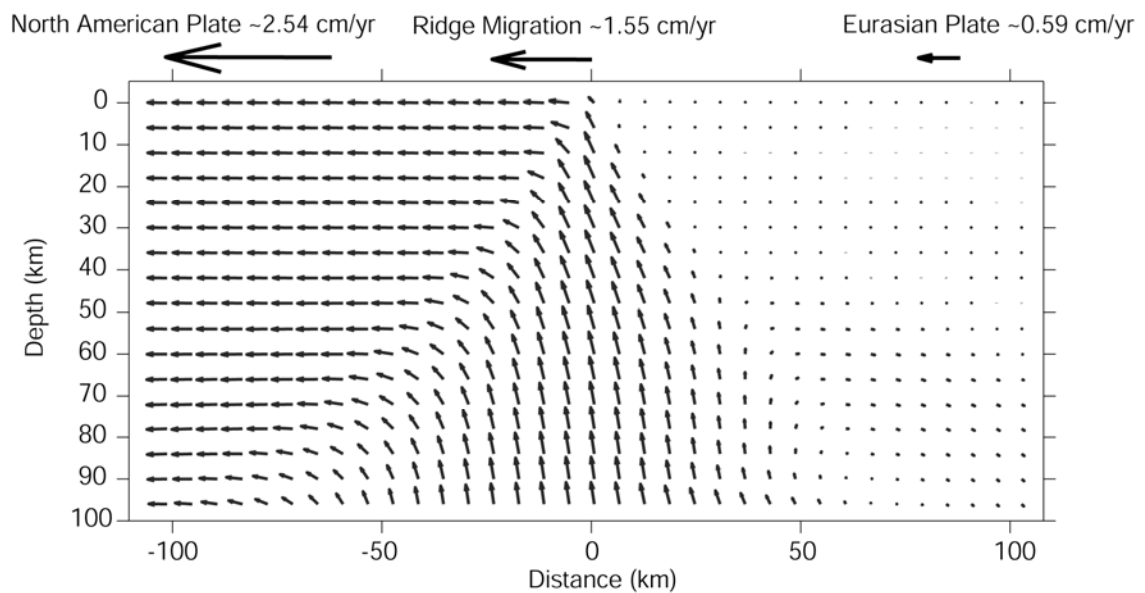


Figure 12. Shown are mantle flow vectors beneath a migrating ridge [Mittelstaedt, *pers. comm.*, 2005] using a purely kinematic model. Using a deep mantle reference frame, the top boundary condition is indicated by the overriding lithospheres of the North American and Eurasian plates. Vectors are components of velocity in the spreading direction. Beneath the Eurasian plate, the mantle is nearly stagnant relative to the lithosphere in the spreading direction, preserving the vertically aligned fast axes of olivine developed in the upwelling zone. Lesser magnitudes of vertically fast anisotropy are preserved beneath the North American Plate due to corner flow and shearing beneath the lithosphere.

FIGURE 13. MANTLE FLOW BENEATH THE REYKJANES RIDGE

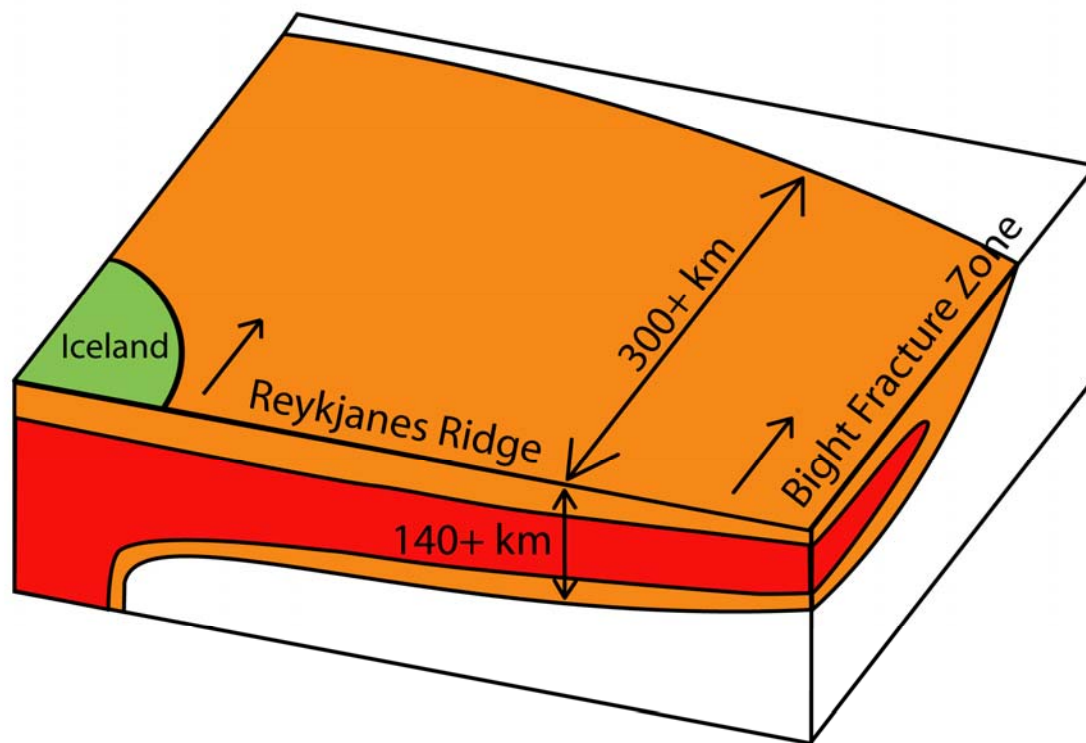


Figure 13. Shown is a cartoon describing how plume material from beneath Iceland disperses in the upper mantle. Minimum dimensions required by the data are shown. The anomaly may extend as far as 500 km from the ridge and up to 200 km in depth. Horizontal flow is not confined to a rheological groove formed by the cooling of the lithosphere away from the ridge.

## APPENDIX A. EARTHQUAKE RADIATION PATTERNS

Since seismograms measured at instruments across Iceland depend on the earthquake source, the initial phase and radiation patterns of the source must be included in the calculation of the synthetic seismograms. Radiation patterns for surface waves are calculated from their moment tensor. A moment tensor is a mathematical representation of the orientation and magnitude of the stresses that generate seismic waves at the earthquake hypocenter. Here, the moment tensor and best double couple solution are taken from the Harvard Seismology Centroid-Moment Tensor Project [*Dziewonski et al.*, 2004]. A simplification of the general moment tensor is often made by assuming the earthquake source is a double couple system of forces acting at a point. Many earthquakes can be approximated by a double couple solution. Figure A-1 shows the focal mechanism of the best double couple solution for earthquakes recorded by the ICEMELT and HOTSPOT instrument arrays.

For the seventeen earthquakes recorded by the ICEMELT and HOTSPOT instrument arrays and two earthquake recorded only by the BORG station of the Global Seismograph Network, the Love wave radiation pattern is similar for both the general moment tensor or the best double couple solution. Furthermore, the effect of source depth on the radiation pattern is insignificant for the ranges considered. Rayleigh wave radiation patterns are more sensitive to the depth of the source and whether one considers a double couple source or general moment tensor. The variation in the radiation pattern and initial phase with depth is most significant for depths above 8-10 km and there are no events more shallow than 8 km. Since there is enough uncertainty in the general

moment tensor and the general tensor does not deviate much from the best double couple solution, the best double couple is a good approximation to describe the source effects of these earthquakes. So, to calculate synthetics, the best double couple solutions are used. The radiation pattern is calculated using equations 7.148 and 7.150 from *Aki and Richards* [2002]. Figures A-2 and A-3 show how the surface wave radiation pattern changes with the depth of the earthquake for two representative earthquakes. Figures A-4 and A-5 show the radiation patterns for Rayleigh waves, with the great circle path from event to station, and initial phase for two representative earthquakes.

## APPENDIX B. INSTRUMENT RESPONSE

The ICEMELT experiment consisted of Streckeisen STS-2 instruments [Bjarnason *et al.*, 1996]. The HOTSPOT experiment consisted of Guralp CMG-3ESP, Guralp CMG-40T, Guralp CMG-3T302, and Guralp CMG-3T instruments [Allen *et al.*, 1999]. Some HOTSPOT stations did not have the same instrument type for the entire duration of the experiment, see table C-1 for details. The BORG station has Streckeisen STS-2 and Geotech KS-54000 instruments [Butler *et al.*, 2004]. In tables C-1 and C-2 the instrument types, locations, and properties are shown for all stations. In figures C-1 to C-5 the instrument responses are plotted. All data comes courtesy of IRIS [IRIS, 2004].

Synthetic waveforms represent ground displacements. The data from both ICEMELT and HOTSPOT instruments are reported in velocity. So, to transform the data from a velocity response to a displacement response, these instrument responses can be modified with an extra zero in the frequency domain, or the signal can be integrated. For HOTSPOT and BORG data, a zero has been added to the instrument responses to convert the ground velocity measurements to ground displacement. For ICEMELT data, the data is integrated to yield ground displacement from ground velocity measurements.

## APPENDIX C. SIGNAL PROCESSING

Signal processing is accomplished using Seismic Analysis Code (SAC) [Goldstein *et al.*, 2004]. The macros described in this appendix are SAC macros, unless otherwise noted. Data collected from the ICEMELT project [Bjarnason *et al.*, 1996] was obtained from a study on the Reykjanes Ridge [Gaherty, 2001]. There is no known previous processing on the data received, and it represents a velocity response. Data collected from the HOTSPOT project and from the BORG station of the Global Seismic Network, was obtained from IRIS [IRIS, 2004] and also represents a velocity response.

1. Macro position.m
  - a. The position, date, and time of the event is updated in the trace header to reflect values from the Bulletin of the International Seismological Center [ISC, 2001].
  - b. The reference time of the trace is set to the event time.
2. Macro rotate.m
  - a. The north (2) and east (3) components are rotated into radial (r) and transverse (t) components, respectively.
3. Macro remove\_ht.m
  - a. The records are cut at 0 and 1000 seconds from the time of the event.
  - b. The mean is removed
  - c. The trend is removed
  - d. Tapering is performed with a 0.1 width Hanning taper.

- e. A low and high pass frequency taper is applied to remove frequencies out of the range of interest. The taper is zero below 0.005 and unity above 0.01 on the low pass. The taper is zero above 1.0 and unity below 0.2 on the high pass.
- f. The instrument response is removed from ICEMELT data using the poles and zeros published by IRIS [IRIS, 2004] for these instruments. See table C-2 in appendix C. ICEMELT data was converted from a velocity response to a displacement response using the SAC transfer program. The instrument response is removed from the HOTSPOT and BORG data using poles and zeros downloaded with the data from IRIS for use in SAC. These poles and zeros are slightly different from those in table C-2 of appendix C. They contain an extra zero to facilitate converting a velocity response to a displacement response.

#### 4. Macro Gabor.m

- a. Gamma is  $267 \times \text{frequency}$  for Love waves. Gamma describes the frequency content of the Gabor wavelets.
- b. Gamma is  $400 \times \text{frequency}$  for Rayleigh waves.
- c. Files are cut at great-circle-distance in km / 7.5 km/s, and great-circle-distance in km / 2.5 km/s. This windows the data around the arrival time of Love and Rayleigh waves.
- d. The mean is removed
- e. The trend is removed

- f. A Hanning taper with width 0.1 is applied
  - g. A Fast Fourier Transform is applied
  - h. A Gabor filter is applied using center frequencies of 0.01, 0.0128, 0.02, 0.03  
0.04, 0.045, 0.05, 0.051 0.053, 0.055, 0.057, 0.059, ...
  - i. With the phase intact, an inverse fast Fourier transform is applied
  - j. The data is decimated by 4
  - k. The means is removed
  - l. The trend is removed
  - m. A Hanning taper with width 0.1 is applied
  - n. Files are written in binary format for plotting and in ASCII format for export  
to Matlab.
5. Macro plotsgf.m
- a. Macro dist.m is called to normalize the traces to a standard velocity model,  
to remove the affect of distance from event to station for plotting purposes.  
Normalized and not normalized traces are retained.
  - b. SGF (SAC graphics file) plots are generated for normalized and not  
normalized traces.
  - c. Shell script convert.c is called to convert the SGF files to postscript files.

## APPENDIX D. INVERSE PROBLEM

As stated in the body of this thesis, the method of Dunn and Forsyth [2003] is used to determine shear wave velocity structure from surface waves. Here, the inverse problem for this method is presented in more detail. Each of the two steps in this method use an equation in the same form. In the first step, the phase delay, amplitude, and group delay of surface waves are used to calculate the surface wave velocity structure as a function of distance from the ridge and frequency. In the second step, the surface wave phase velocities are used to calculate the anisotropic shear wave velocity structure as a function of distance from the ridge and depth. For this non-linear problem, the solution at the  $n+1$  iteration is determined by Tarantola [1987]:

$$m_{n+1} = m_n - \left[ \left( G_n^t C_d^{-1} G_n + C_m^{-1} \right)^{-1} \left( G_n^t C_d^{-1} (g(m_n) - d_{obs}) + C_m^{-1} (m_n - m_{prior}) \right) \right]$$

where  $m_{prior}$  is the starting model and includes the coefficients of the dispersion curve at each control node of the spline, the amplitude scaling factors, and the event location parameters;  $m_n$  is the solution at the  $n^{\text{th}}$  iteration; the covariance operator  $C_m$  describes the uncertainties of the starting model;  $d_{obs}$  is the vector of observed data values with uncertainties described by the covariance operator  $C_d$ ;  $g(m_n)$  is the predicted data from the  $n^{\text{th}}$  iteration of the forward problem; and  $G_n$  is the matrix of partial derivatives relating changes in  $g(m_n)$  to changes in model values.  $G_n$  is determined numerically by making small perturbations ( $\delta m$ ) to  $m_n$  and calculating the changes  $g(m_n + \delta m)$  at the start of each iteration.

For the first step in this method,  $G_n$  can be broken down as:

$$G = \begin{bmatrix} G^G \\ G^A \\ G^P \end{bmatrix}$$

where the superscripts G, A, and P represent the covariance for each of the modeled wave parameters: group delay, amplitude, and phase delay. The data covariance matrix, using the same superscripts as G, is written as:

$$C_d = \begin{bmatrix} C_d^G & 0 & 0 \\ 0 & C_d^A & 0 \\ 0 & 0 & C_d^P \end{bmatrix}$$

The *a priori* model covariance matrix is written as:

$$C_d = \begin{bmatrix} C_m^a & 0 & 0 \\ 0 & C_m^M & 0 \\ 0 & 0 & C_m^P \end{bmatrix}$$

where the superscripts a, M, and R indicate the covariance for the model parameters that describe the phase velocity, the scale factors for the event magnitudes, and the changes to earthquake positions.

For the second step in this method  $d_{\text{obs}}$  are the dispersion curves calculated in the first step,  $m_n$  is the shear wave model at the  $n^{\text{th}}$  iteration,  $g(m_n)$  are dispersion curves for model  $m_n$ , and  $G_n$  contains partial derivatives relating changes in phase velocity to changes in shear velocity as determined by Saito's routine [Saito, 1988].

TABLE A-1. ICEMELT EVENT PARAMETERS

Table A-1. Earthquakes recorded by the ICEMELT instrument array. Data is from the Harvard CMT Project [Dziewonski *et al.*, 2004], the Engdahl catalog [Engdahl *et al.*, 1998], and the International Seismological Centre [ISC, 2001]. For moment tensor data, the Aki and Richards format is used [Aki and Richards, 2002], [Yomogida and Aki, 1985], (Mxx=North, Myy=East, Mzz=Down). The Harvard CMT Project format is (Mrr=Up, Mtt=South, Mpp=East). The following equalities apply: (Mxx=Mtt, Myy=Mpp, Mzz=Mrr, Mxy=-Mtp, Myz=-Mrp, Mxz=Mrt).

Number	Harvard	Date	ISC Time	ISC Lat	ISC Lon	Engdahl Depth	Ms
942251424	081394B	1994/8/13	14:24:33.3600	54.1425	-35.1426	18.8	4.5
952051913	072495C	1995/7/24	19:13:21.5800	55.532	-35.0955	18.8	5.2
953181618	111495F	1995/11/14	16:18:51.1100	52.6187	-32.3296	22.2	4.2
953512348	121795B	1995/12/17	23:48:31.5800	52.6722	-32.1233	13.3	4.8
960802222	032096C	1996/3/20	22:22:43.6600	51.0528	-30.0581	26.6	4.7
961021051	041196B	1996/4/11	10:51:15.2300	56.9804	-33.7683	18	4.7
961600526	060896B	1996/6/8	05:26:10.4900	58.3526	-31.9797	47.7	4.8

Table A-1 (Continued) Moment tensor

Number	Exp	Mxx	Mxx err	Myy	Myy err	Mzz	Mzz err	Mxy	Mxy err	Myz	Myz err	Mxz	Mxz err
942251425	23	1.16	0.66	2.41	0.43	-3.58	0.38	0.81	0.37	0	0.00	0.00	0.00
952051913	24	0.20	0.04	0.85	0.04	-1.05	0.03	-0.24	0.06	0	0.00	0.00	0.00
953181618	23	-1.22	0.51	1.48	0.50	-0.26	0.28	5.72	0.29	0	0.00	0.00	0.00
953512348	24	-0.11	0.10	0.44	0.09	-0.33	0.07	1.99	0.07	-0.52	0.28	-1.03	0.28
960802222	23	-2.08	0.62	5.76	0.46	-3.69	0.47	0.67	0.49	-5.79	1.60	0.70	1.16
961021051	23	0.71	3.00	3.18	0.97	-3.89	2.11	-2.04	0.95	0	0.00	0.00	0.00
961600526	23	-1.93	1.08	5.62	0.51	-3.69	0.67	-0.92	0.48	0.97	2.50	1.71	1.44

Table A-1 (Continued) Best double-couple

Number	Strike1	Dip1	Slip1	Strike2	Dip2	Slip2
942251425	334	45	-90	154	45	-90
952051913	199	45	-90	19	45	-90
953181618	277	90	-180	7	90	0
953512348	6	62	2	275	88	152
960802222	335	22	-121	187	71	-78
961021051	209	45	-90	29	45	-90
961600526	215	49	-46	339	57	-129

TABLE A-2. HOTSPOT EVENT PARAMETERS

Table A-2. Earthquakes recorded by the HOTSPOT instrument array. Data is from the Harvard CMT Project [*Dziewonski et al.*, 2004], the Engdahl catalog [*Engdahl et al.*, 1998], and the International Seismological Centre [*ISC*, 2001]. For moment tensor data, the Aki and Richards format is used [*Aki and Richards*, 2002], [*Yomogida and Aki*, 1985], ( $M_{xx}$ =North,  $M_{yy}$ =East,  $M_{zz}$ =Down). The Harvard CMT Project format is ( $M_{rr}$ =Up,  $M_{tt}$ =South,  $M_{pp}$ =East). The following equalities apply: ( $M_{xx}$ = $M_{tt}$ ,  $M_{yy}$ = $M_{pp}$ ,  $M_{zz}$ = $M_{rr}$ ,  $M_{xy}$ = $-M_{tp}$ ,  $M_{yz}$ = $-M_{rp}$ ,  $M_{xz}$ = $M_{rt}$ ).

Number	Harvard	Date	ISC Time	ISC Lat	ISC Lon	Engdahl Depth	Ms
970930517	040397C	1997/4/3	05:17:25.0400	57.165	-33.6393	14.6	4.8
971901447	070997B	1997/7/9	14:47:17.1900	52.2588	-31.5156	14.3	4.9
972401110	082897A	1997/8/28	11:10:07.6300	57.0383	-33.8645	19.5	5.2
980450654	021498B	1998/2/14	06:54:19.4000	52.5593	-32.6514	21.4	4.9
980471336	021698A	1998/2/16	13:36:15.7400	52.6204	-33.7762	15	4.9
980472353	021698C	1998/2/16	23:53:19.9400	52.6815	-33.6622	8	6.6
980561905	022598C	1998/2/25	19:05:51.9100	53.9275	-35.2276	16.8	5.5
980572314	022698D	1998/2/26	23:14:38.3500	54.044	-35.2541	11.4	4.9
981760215	062598A	1998/6/25	02:15:48.7900	52.7136	-34.7905	25.1	4.7

Table A-1 (Continued) Moment tensor

Number	Harvard	exp	Mxx	Mxx err	Myy	Myy err	Mzz	Mzz err	Mxy	Mxy err	Myz	Myz err	Mxz	Mxz err
970930517	040397C	23	1.17	0.82	6.26	0.52	-7.43	0.46	-2.43	0.38	1.7	2.6	-0.81	1.5
971901447	070997B	24	-0.05	0.03	0.41	0.04	-0.36	0.03	1.3	0.03	0	0	0	0
972401110	082897A	24	0.24	0.04	0.87	0.04	-1.11	0.03	-0.42	0.04	-0.29	0.2	0.06	0.13
980450654	021498B	24	-0.09	0.05	0.43	0.05	-0.34	0.04	1.51	0.05	0.18	0.19	0.41	0.14
980471336	021698A	24	-0.17	0.04	0.38	0.04	-0.21	0.03	1.53	0.03	-0.08	0.13	0.73	0.11
980472353	021698C	26	-0.23	0	0.33	0.01	-0.09	0	1.31	0	-0.24	0.03	0.55	0.02
980561905	022598C	24	0.11	0.05	2.18	0.06	-2.29	0.04	0.04	0.05	-0.83	0.21	1.75	0.14
980572314	022698D	23	0.54	0.67	3.2	0.5	-3.74	0.38	-1.18	0.4	0	0	0	0
981760215	062598A	23	1.94	0.49	5.18	0.36	-7.12	0.38	0.94	0.47	4.55	1.77	9.03	1.2

Table A-1 (Continued) Best double-couple

Number	Strike1	Dip1	Slip1	Strike2	Dip2	Slip2
970930517	201	38	-91	23	52	-89
971901447	275	90	-180	5	90	0
972401110	30	38	-85	203	52	-94
980450654	185	75	0	275	90	-165
980471316	183	65	-8	277	83	-155
980472353	184	70	-11	278	80	-159
980561905	341	38	-132	209	63	-62
980572314	201	45	-90	21	45	-90
981760215	162	18	-55	305	75	-101

TABLE A-3. BORG EVENT PARAMETERS

Table A-3. Earthquakes recorded by the BORG station of the GSN. Data is from the Harvard CMT Project [Dziewonski *et al.*, 2004], the Engdahl catalog [Engdahl *et al.*, 1998], and the International Seismological Centre [ISC, 2001]. For moment tensor data, the Aki and Richards format is used [Aki and Richards, 2002], [Yomogida and Aki, 1985], (Mxx=North, Myy=East, Mzz=Down). The Harvard CMT Project format is (Mrr=Up, Mtt=South, Mpp=East). The following equalities apply: (Mxx=Mtt, Myy=Mpp, Mzz=Mrr, Mxy=-Mtp, Myz=-Mrp, Mxz=Mrt).

Number	Harvard	Date	ISC Time	ISC Lat	ISC Lon	Engdahl Depth	Ms
002211757	080800C	2000/8/8	17:57:42.27	62.4630	-25.8040	15	4.9
982870136	101498A	1998/10/14	01:36:20.09	60.6616	-44.0581	32.7	4.4

Table A-3 (Continued) Moment tensor

Number	exp	Mxx	Mxx err	Myy	Myy err	Mzz	Mzz err	Mxy	Mxy err	Myz	Myz err	Mxz	Mxz err
002211757	24	0.169	0.046	0.155	0.049	-0.324	0.034	-1.224	0.038	0.103	0.147	-0.064	0.119

Table A-3 (Continued) Best double-couple

Number	strike1	dip1	slip1	strike2	dip2	slip2
002211757	270	86	1	180	89	176

TABLE B-1. INSTRUMENT LOCATIONS AND TYPES

Table B-1. Instruments using channels BHZ,BHN,BHE.

Number	Network	Station	Date Start	Time Start	Date End	Time End	Latitude	Longitude	Station Type
1	HOTSPOT	HOT16	1996-07-14	15:53:21.0	1998-08-13	13:39:11.0	65.540825	-13.753478	CMG3ESP
2	HOTSPOT	HOT19	1996-07-20	16:56:25.0	1998-08-16	14:51:04.0	64.810371	-14.090622	CMG3ESP
3	HOTSPOT	HOT17	1996-07-10	17:03:27.0	1998-08-13	19:14:05.0	65.256226	-14.501803	CMG3ESP
4	ICEMELT	birh					65.007300	-14.618900	STS-2
5	HOTSPOT	HOT29	1996-07-22	18:12:26.0	1998-08-12	14:25:26.0	65.728622	-14.873623	CMG40T
6	ICEMELT	asbs					65.704700	-14.917100	STS-2
7	HOTSPOT	HOT20	1996-07-03	09:57:17.0	1997-04-24	21:35:23.0	64.287781	-15.139223	CMG3ESP
7	HOTSPOT	HOT20	1997-04-24	21:59:28.0	1997-06-10	11:15:04.0	64.287781	-15.139223	CMG3ESP
7	HOTSPOT	HOT20	1997-06-10	12:28:44.0	1998-07-30	16:55:12.0	64.287781	-15.139223	CMG3ESP
8	HOTSPOT	HOT15	1996-07-14	16:14:37.0	1997-02-13	19:42:27.0	66.121422	-15.169086	CMG3ESP
8	HOTSPOT	HOT15	1997-05-07	18:51:00.0	1998-08-12	11:10:54.0	66.121422	-15.169086	CMG3ESP
9	HOTSPOT	HOT18	1996-07-09	17:17:55.0	1998-08-14	18:44:19.0	65.165932	-15.308651	CMG3ESP
10	ICEMELT	hoff					64.396700	-15.340400	STS-2
11	HOTSPOT	HOT24	1996-07-16	20:43:18.0	1996-08-11	18:05:13.0	64.886208	-15.353522	CMG3ESP
11	HOTSPOT	HOT24	1996-08-11	18:09:01.0	1996-08-11	18:09:51.0	64.886208	-15.353522	CMG3ESP
11	HOTSPOT	HOT24	1996-08-11	18:10:51.0	1998-03-19	09:57:38.0	64.886208	-15.353522	CMG3ESP
11	HOTSPOT	HOT24	1998-03-19	10:26:55.0	1998-08-14	10:58:57.0	64.886208	-15.353522	CMG3ESP
12	ICEMELT	bre					66.289600	-16.425300	STS-2
13	HOTSPOT	HOT21	1996-07-02	17:41:16.0	1996-07-08	15:32:29.0	63.876549	-16.641010	CMG3ESP
13	HOTSPOT	HOT21	1996-07-08	16:23:41.0	1996-11-11	15:55:16.0	63.876549	-16.641010	CMG3ESP
13	HOTSPOT	HOT21	1996-11-11	15:55:16.0	1996-11-11	18:57:57.0	63.876549	-16.641010	CMG3ESP
13	HOTSPOT	HOT21	1996-11-17	11:26:02.0	1998-07-31	09:07:07.0	63.876549	-16.641010	CMG3ESP
14	HOTSPOT	HOT25	1996-07-19	18:03:54.0	1997-09-25	19:54:30.0	65.054375	-16.650196	CMG40T
14	HOTSPOT	HOT25	1997-09-26	09:26:13.0	1998-05-09	03:08:08.0	65.054375	-16.650196	CMG40T
15	ICEMELT	askj					64.984400	-16.675400	STS-2
16	ICEMELT	skot					65.341200	-17.246700	STS-2
17	HOTSPOT	HOT23	1996-07-27	20:33:39.0	1996-07-28	11:07:15.0	64.406776	-17.266495	CMG3ESP
17	HOTSPOT	HOT23	1996-07-28	11:26:21.0	1996-10-12	17:00:23.0	64.406776	-17.266495	CMG3ESP
17	HOTSPOT	HOT23	1996-10-12	17:07:11.0	1996-10-23	10:26:35.0	64.406776	-17.266495	CMG3ESP
17	HOTSPOT	HOT23	1997-01-13	07:31:00.0	1997-01-13	07:31:28.0	64.406776	-17.266495	CMG3ESP
17	HOTSPOT	HOT23	1997-01-13	11:09:13.0	1997-04-12	09:30:48.0	64.406776	-17.266495	CMG3ESP
17	HOTSPOT	HOT23	1997-05-17	10:39:55.0	1997-07-19	19:31:38.0	64.406776	-17.266495	CMG3ESP
17	HOTSPOT	HOT23	1997-09-07	10:56:29.0	1998-08-12	13:19:17.0	64.406776	-17.266495	CMG3ESP
18	ICEMELT	kar					63.946500	-17.686200	STS-2
19	ICEMELT	nyd					64.734500	-18.068800	STS-2
20	HOTSPOT	HOT13	1996-06-22	13:49:20.0	1998-08-11	14:45:06.0	65.685928	-18.099773	CMG3T302
21	ICEMELT	akud					65.685900	-18.099900	STS-2
22	HOTSPOT	HOT22	1996-07-02	15:16:20.0	1996-11-18	15:11:34.0	63.769817	-18.130611	CMG3ESP
22	HOTSPOT	HOT22	1996-11-18	15:11:35.0	1996-11-18	20:35:41.0	63.769817	-18.130611	CMG3ESP
22	HOTSPOT	HOT22	1996-12-02	16:10:18.0	1998-07-31	13:24:03.0	63.769817	-18.130611	CMG3ESP
23	HOTSPOT	HOT14	1996-06-22	11:00:01.0	1998-08-09	16:22:32.0	65.302811	-18.256500	CMG3ESP
24	HOTSPOT	HOT26	1996-07-25	10:15:44.0	1998-08-09	11:21:19.0	65.027626	-18.331696	CMG3ESP
25	ICEMELT	ljop					64.024900	-19.020100	STS-2
26	HOTSPOT	HOT28	1996-07-03	15:51:57.0	1997-10-28	13:35:49.0	64.532478	-19.484184	CMG40T
26	HOTSPOT	HOT28	1997-10-28	13:43:06.0	1998-08-01	15:31:59.0	64.532478	-19.484184	CMG40T
27	HOTSPOT	HOT12	1996-06-21	15:57:15.0	1996-08-27	09:21:13.0	65.670700	-19.599640	CMG3T
27	HOTSPOT	HOT12	1996-08-27	09:52:16.0	1998-08-10	21:39:59.0	65.670700	-19.599640	CMG3ESP
28	HOTSPOT	HOT27	1996-07-31	15:22:47.0	1998-08-10	13:38:57.0	65.225365	-19.673590	CMG3ESP
29	ICEMELT	blol					65.231000	-19.717800	STS-2
30	ICEMELT	hrau					66.118600	-20.098700	STS-2
31	HOTSPOT	HOT11	1996-06-22	20:02:08.0	1996-08-26	20:00:02.0	65.422218	-20.721770	CMG3T
31	HOTSPOT	HOT11	1996-08-26	21:04:25.0	1996-12-25	04:05:47.0	65.422218	-20.721770	CMG3ESP
31	HOTSPOT	HOT11	1997-01-02	17:01:38.0	1998-08-10	18:20:48.0	65.422218	-20.721770	CMG3ESP
32	HOTSPOT	HOT05	1996-06-25	12:58:10.0	1996-08-04	14:53:18.0	65.109688	-21.096394	CMG3ESP
32	HOTSPOT	HOT05	1996-08-04	15:09:31.0	1998-07-29	10:19:40.0	65.109688	-21.096394	CMG3ESP
33	HOTSPOT	HOT01	1996-06-19	15:24:18.0	1998-07-26	06:29:07.0	64.494139	-21.167883	CMG3ESP
34	GSN	BORG	1994-07-31	00:00:00.0	1995-02-09	23:59:59.0	64.747400	-21.326800	STS-2
34	GSN	BORG	1995-02-15	00:00:00.0	2003-08-28	23:59:59.0	64.747400	-21.326800	STS-2
35	GSN	BORG	1994-07-31	00:00:00.0	1995-02-15	00:00:00.0	64.747400	-21.326800	Geotech KS-54000
35	GSN	BORG	1995-02-15	00:00:00.0	2002-05-21	00:00:00.0	64.747400	-21.326800	Geotech KS-54000
36	ICEMELT	klu					65.782000	-21.518000	STS-2
37	HOTSPOT	HOT06	1996-06-25	16:36:29.0	1996-08-04	17:04:07.0	65.705025	-21.677841	CMG3ESP
37	HOTSPOT	HOT06	1996-08-04	17:21:51.0	1996-10-25	15:30:13.0	65.705025	-21.677841	CMG3ESP
37	HOTSPOT	HOT06	1996-10-25	15:30:13.0	1996-10-25	20:52:21.0	65.705025	-21.677841	CMG3ESP
37	HOTSPOT	HOT06	1996-11-03	20:47:51.0	1998-08-08	12:29:44.0	65.705025	-21.677841	CMG3ESP
38	HOTSPOT	HOT30	1996-08-06	15:56:14.0	1996-08-12	11:25:15.0	64.127670	-21.903950	CMG3ESP

TABLE B-2. INSTRUMENT POLES AND ZEROS

Table B-2. Instrument Poles and Zeros [*IRIS*, 2004].

Instrument	Poles	Zeros	Normalizing Factor	Natural Period
STS-2	$-3.701E-02 + 3.701E-02i$	0	5.920E+07	120s
	$-3.70E-02 - 3.701E-02i$	0		
	$-2.51E+02$			
	$-1.310E+02 + 4.673E+02i$			
	$-1.310E+02 - 4.673E+02i$			
CMG-3ESP, CMG-40T	$-0.1481+0.1418i$	0	1.00E+00	30s
	$-0.1481-0.1418i$	0		
CMG-3T	$-3.701E-02 + 3.701E-02i$	0	5.730E+08	120s
	$-3.701E-02 - 3.701E-02i$	0		
	$-1.131E+03$			
	$-1.005E+03$			
	$-5.027E+02$			
CMG-3T302	$-4.443E-02 + 4.443E-02i$	0	1.00E+00	
	$-4.443E-02 - 4.443E-02i$	0		

FIGURE A-1. EVENT FOCAL MECHANISMS

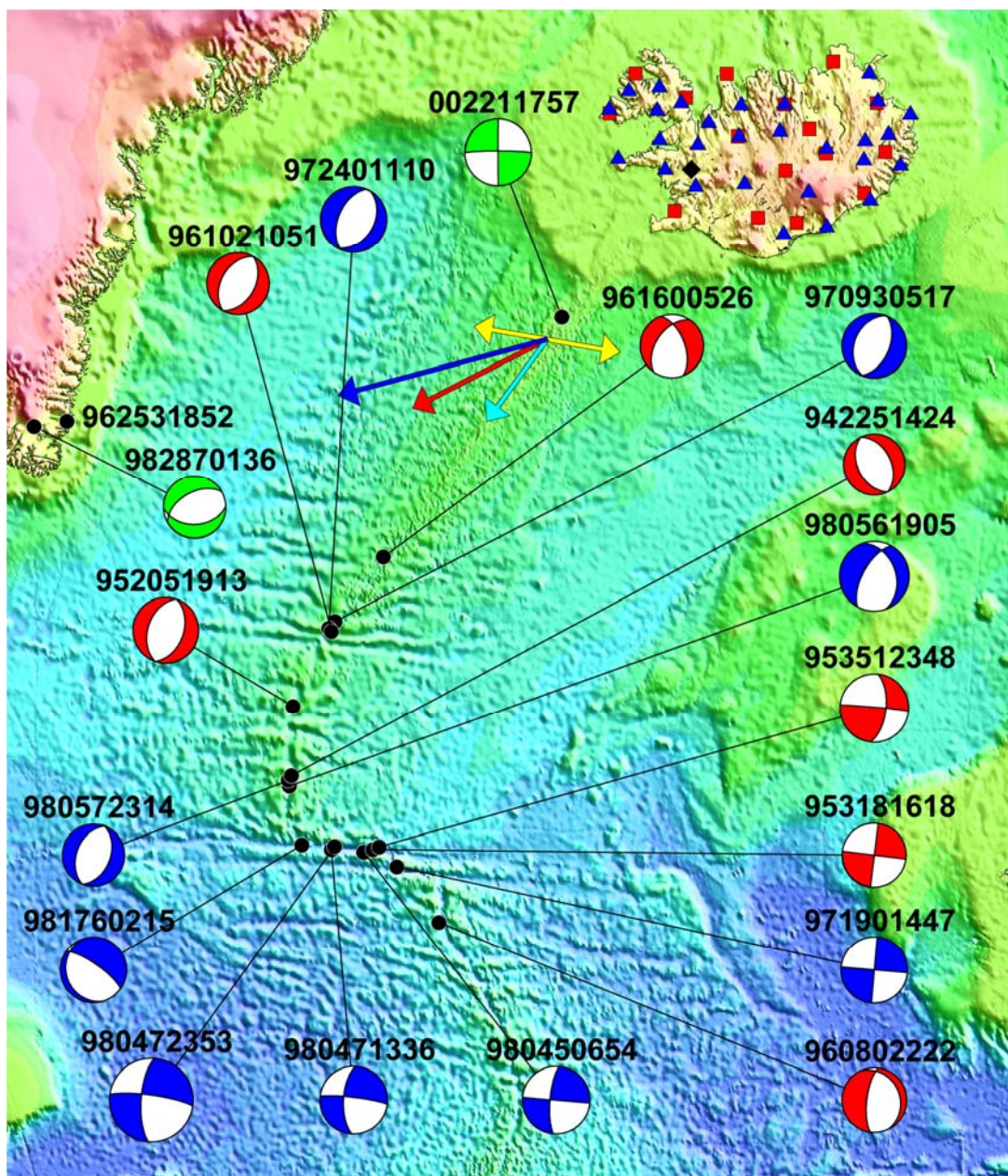


Figure A-1. Shown are the focal mechanisms for the best double couple solution for earthquakes recorded by the ICEMELT and HOTSPOT instrument arrays. Red beach balls and red squares indicate ICEMELT earthquakes and stations. Blue beach balls and blue triangles indicate HOTSPOT earthquakes and stations. The green beach ball and green diamond shows the BORG station and an earthquake recorded only by the BORG station. The yellow arrows indicate relative plate motion; light blue indicates absolute motion of the Eurasian plate in a hotspot reference frame; dark blue indicates absolute motion of the North American Plate; red indicates the absolute motion of the plate

boundary.

FIGURE A-2. RADIATION PATTERN VERSUS DEPTH

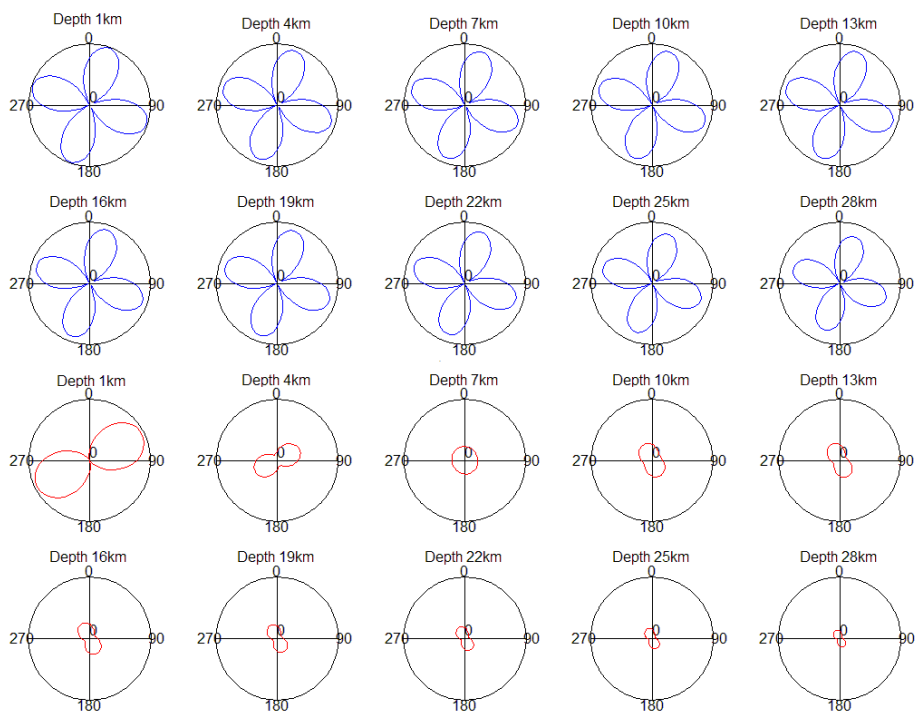


Figure A-2. The variation of the radiation pattern with depth for event 942251424. The blue curves at the top are Love wave radiation patterns. The red curves at the bottom are Rayleigh wave radiation patterns.

FIGURE A-3. RADIATION PATTERN VERSUS DEPTH

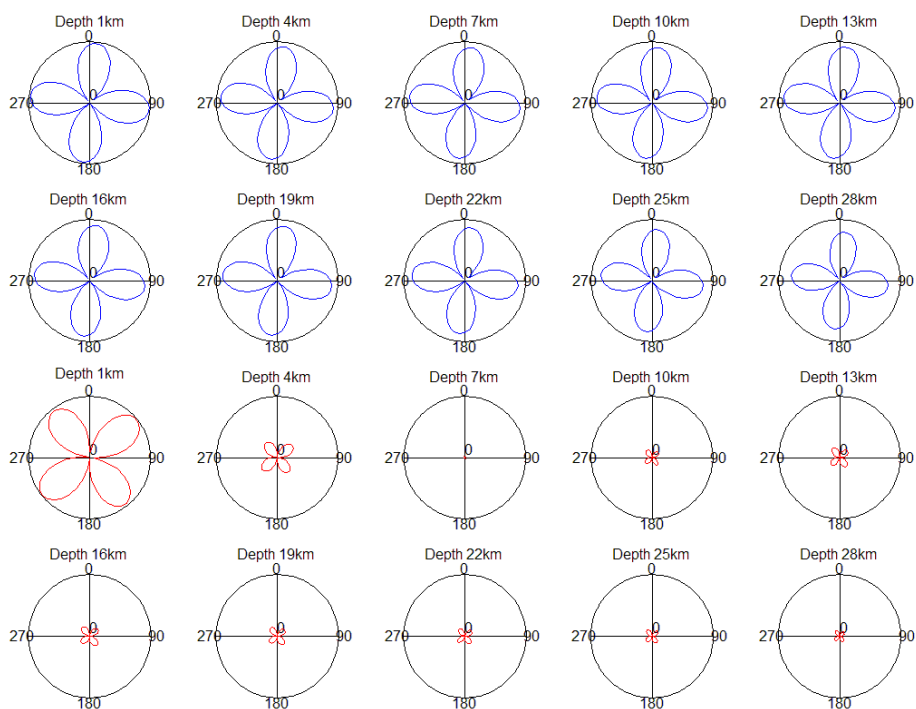


Figure A-3. The variation of the radiation pattern with depth for event 953181618. The blue curves at the top are Love wave radiation patterns. The red curves at the bottom are Rayleigh wave radiation patterns.

FIGURE A-4. RADIATION PATTERN AND INITIAL PHASE

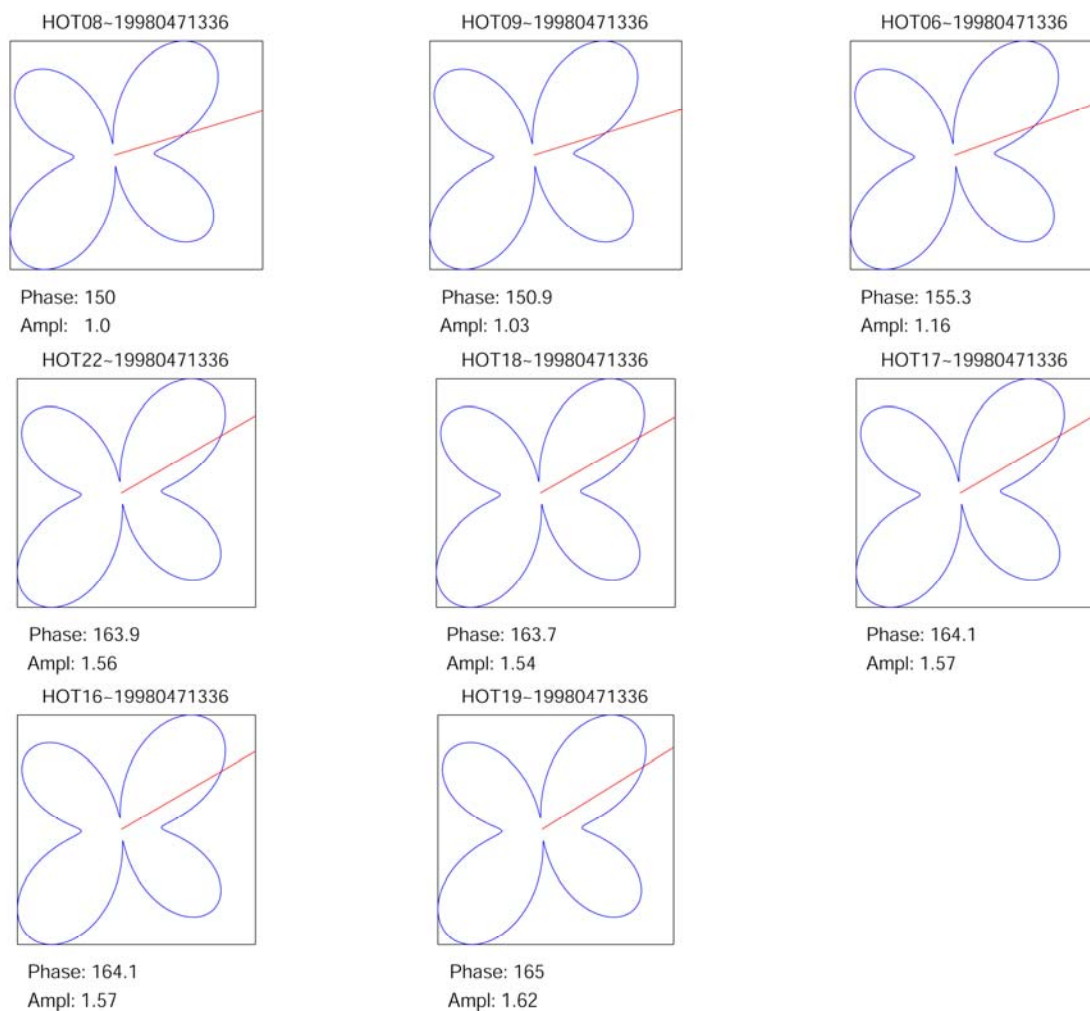


Figure A-4. The radiation pattern for Rayleigh waves used in the phase velocity inversion for a representative event. The red line represents the great circle path for the indicated event-station pair. Above each image are the station and event names. Under each image are the amplitude ratio and the initial phase.

FIGURE A-5. RADIATION PATTERN AND INITIAL PHASE

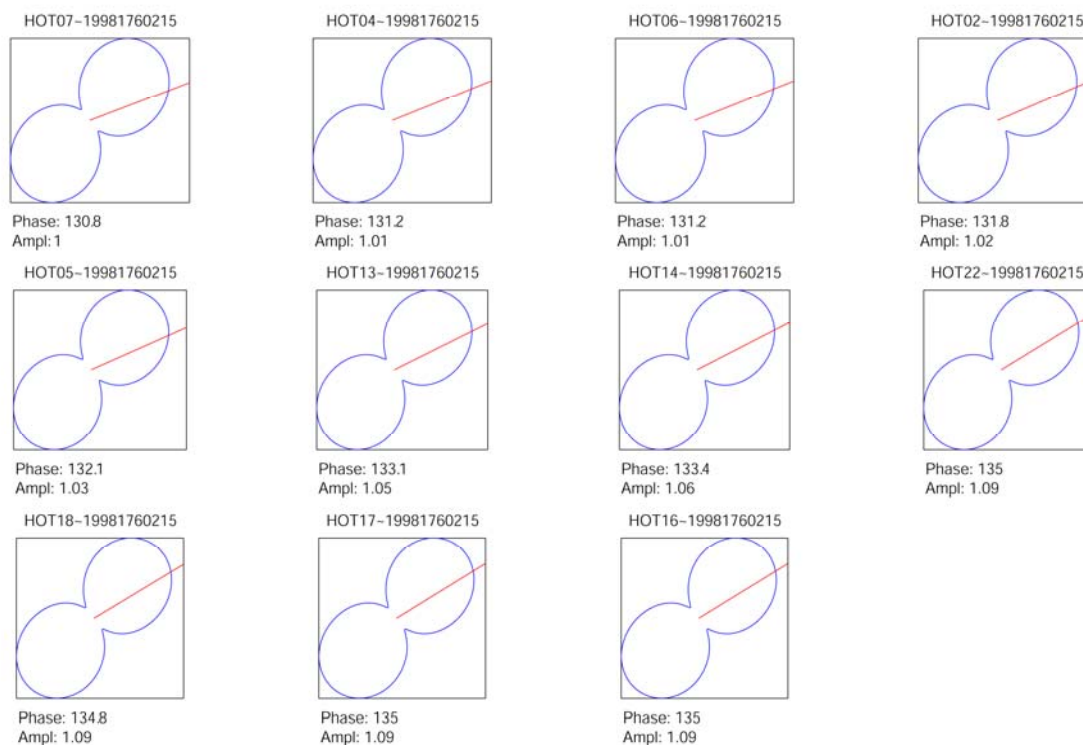


Figure A-5. The radiation pattern for Rayleigh waves used in the phase velocity inversion for a representative event. The red line represents the great circle path for the indicated event-station pair. Above each image are the station and event names. Under each image are the amplitude ratio and the initial phase.

FIGURE B-1. STS-2 INSTRUMENT RESPONSE FROM MANUFACTURER

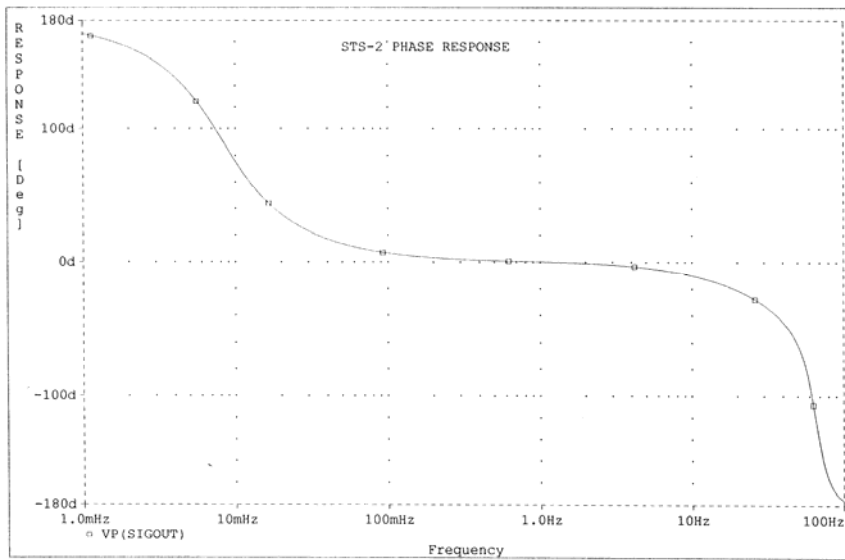
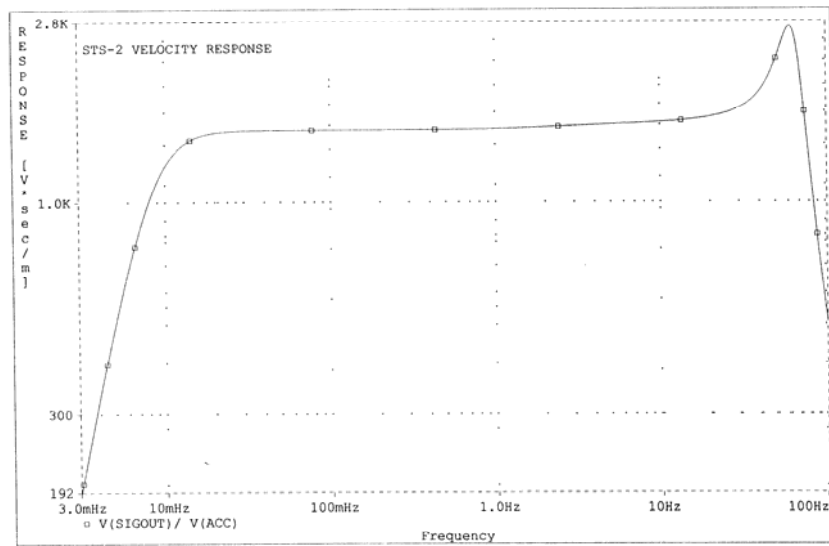


Figure B-1. Instrument response for STS-2 according to the manufacturer.

FIGURE B-2. STS-2 INSTRUMENT RESPONSE FROM POLES AND ZEROS

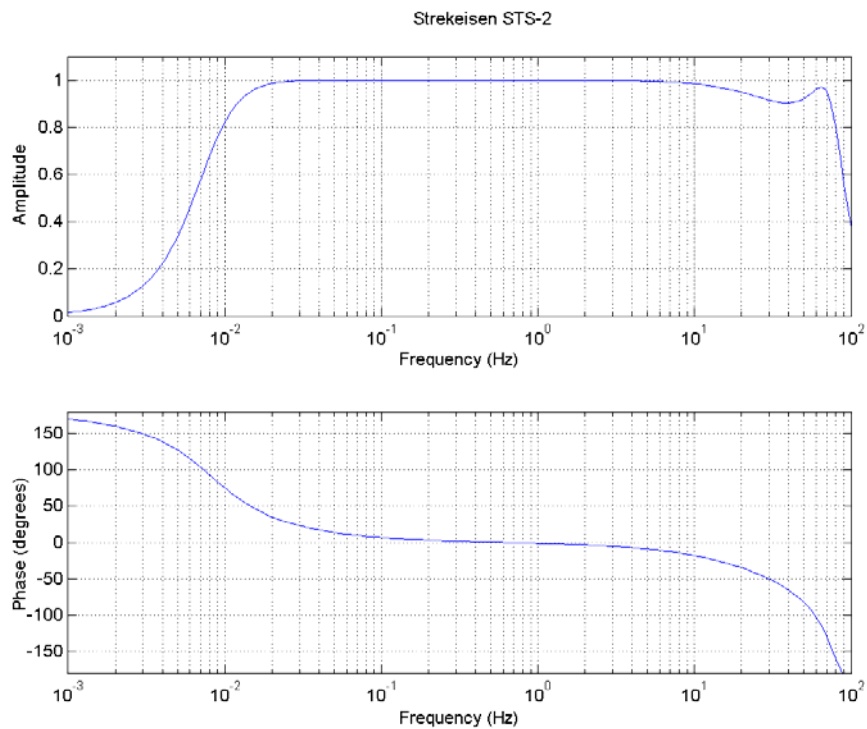


Figure B-2. Instrument response for Strekeisen STS-2, according to calculations from poles and zeros.

FIGURE B-3. GURALP CMG-3T302 INSTRUMENT RESPONSE

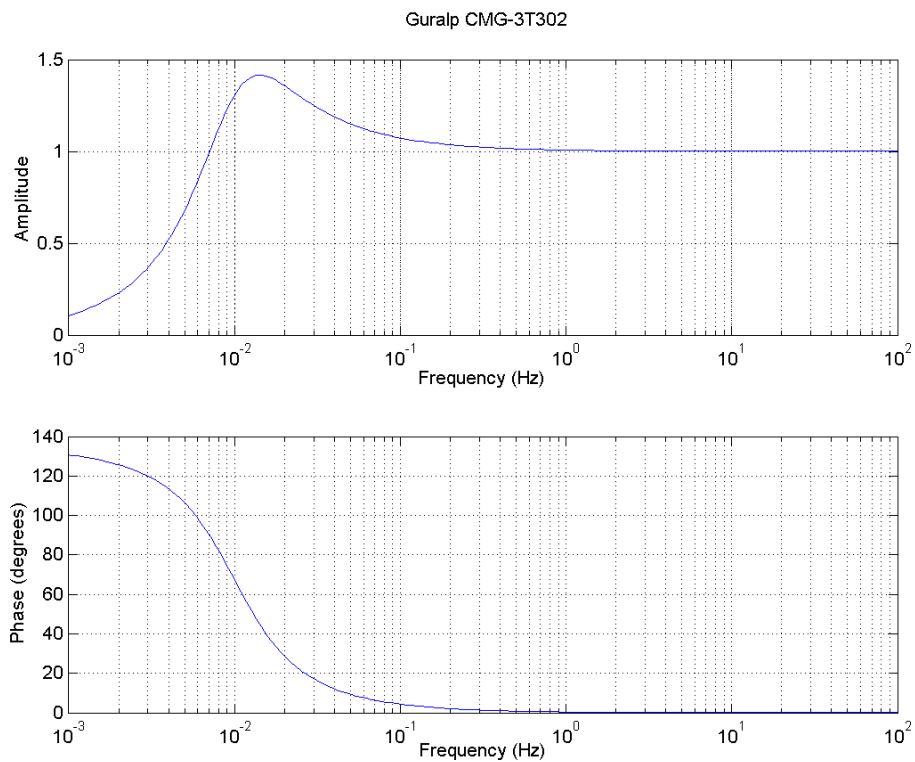


Figure B-3. Instrument responses for Guralp CMG-3T302 according to calculations from poles and zeros.

FIGURE B-4. GURALP CMG-3T INSTRUMENT RESPONSE

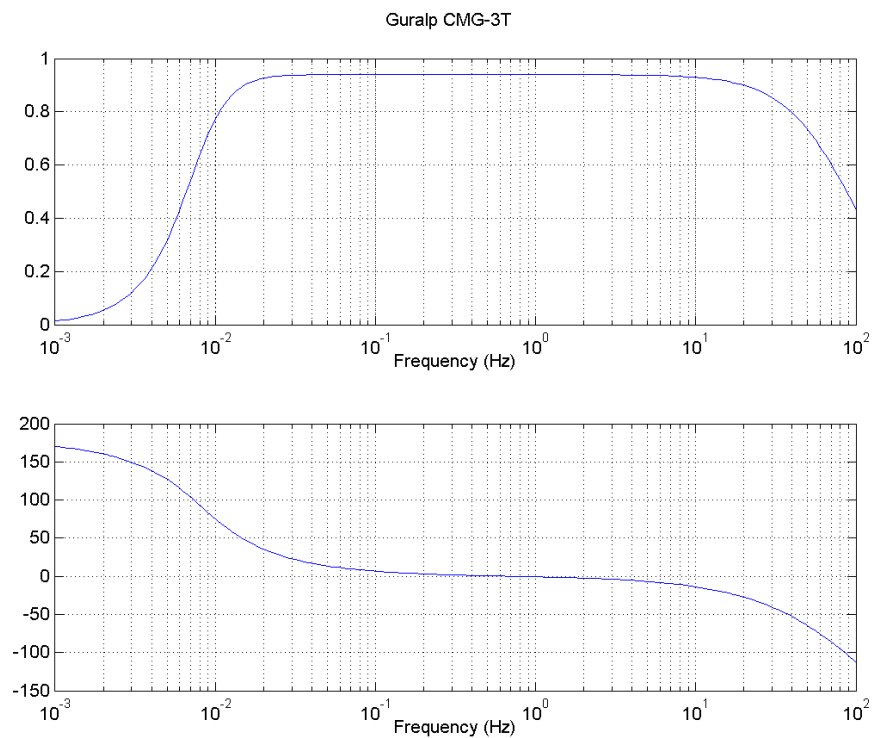


Figure B-4. Instrument response for Guralp CMG-3T, according to calculations from poles and zeros.

FIGURE B-5. GURALP CMG-3ESP AND CMG-40T INSTRUMENT RESPONSES

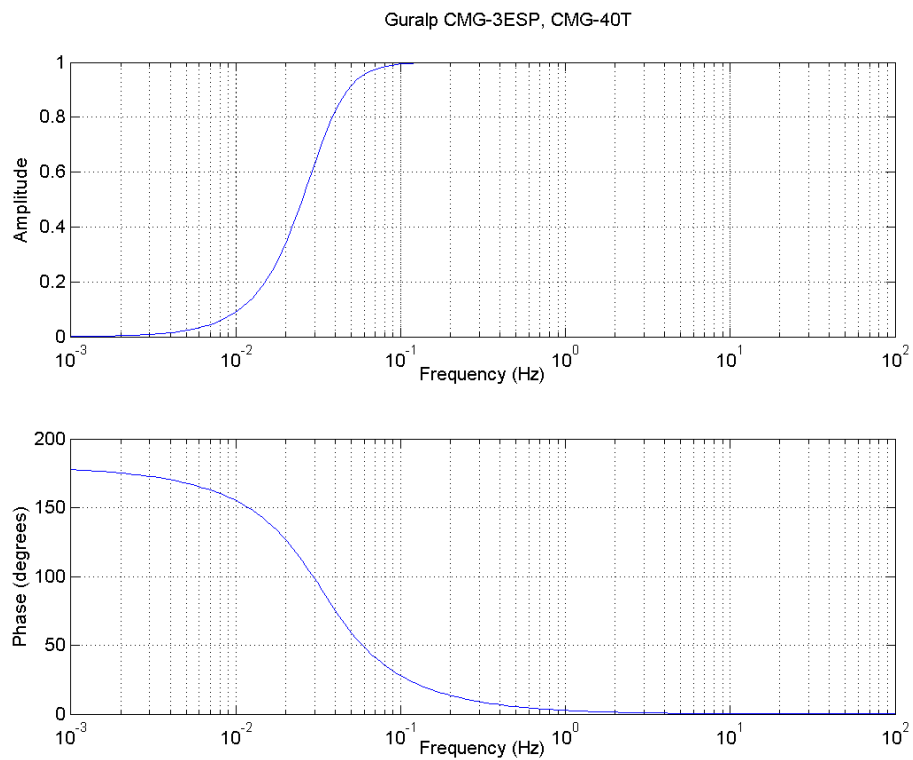


Figure B-5. Instrument response for Guralp CMG-3ESP and CMG-40T, according to calculations from poles and zeros.

## REFERENCES

- National Geophysical Data Center (1993), 5-Minute Gridded Global Relief Data on CD-ROM (ETOPO5), Data Announcement 93-MGG-01, Colorado, USA.
- International Seismological Centre (2001), On-line Bulletin, International Seismological Centre, Thatcham, United Kingdom.
- Incorporated Research Institutions for Seismology (2004), IRIS DMS, Data Management System, Seattle, WA.
- National Geophysical Data Center (2005), Total Sediment Thickness of the World's Oceans & Marginal Seas, Colorado, USA.
- Aki, K., and P.G. Richards (2002), *Quantitative Seismology*, University Science Books.
- Albers, M., and U. Christensen, R. (2001), Channeling of plume flow beneath mid-ocean ridges, *Earth and Planetary Science Letters*, 187, 207-220,
- Allen, R.M., G. Nolet, J.P. Morgan, K. Vogfjord, B.H. Bergsson, P. Erlendsson, G.R. Foulger, S. Jakobsdottir, B.R. Julian, M. Pritchard, S. Ragnarsson, and R. Stefansson (2002), Imaging the mantle beneath Iceland using integrated seismological techniques, *Journal of Geophysical Research*, 107(12),
- Allen, R.M., G. Nolet, W.J. Morgan, K. Vogfjord, B.H. Bergsson, P. Erlendsson, G.R. Foulger, S. Jakobsdottir, B.R. Julian, M. Pritchard, S. Ragnarsson, and R. Stefansson (1999), The thin hot plume beneath Iceland, *Geophysical Journal International*, 137(1), 51-63,
- Babuska, V., and M. Cara (1991), *Seismic anisotropy in the Earth, Vol. 10*, Modern Approaches in Geophysics, Kluwer Academic Publishers, Dordrecht, Netherlands.
- Barclay, A.H., D.R. Toomey, and S.C. Solomon (2001), Microearthquake characteristics and crustal Vp/Vs structure at the Mid-Atlantic Ridge, 35 degrees N, *Journal of Geophysical Research*, B106, 2017-2034,
- Bijwaard, H., and W. Spakman (1998), Closing the gap between regional and global travel time tomography, *Journal of Geophysical Research*, 103, 30055-30078,
- Bijwaard, H., and W. Spakman (1999), Tomographic evidence for a narrow whole mantle plume below Iceland, *Earth and Planetary Science Letters*, 166(121-126),
- Bjarnason, I.T., C.J. Wolfe, S.C. Solomon, and G.B. Gudmundsson (1996), Initial results from the ICEMELT experiment: Body-wave delay times and shear-wave splitting across Iceland, *Geophysical Research Letters*, 23(5), 459-462,
- Braun, M.G., G. Hirth, and E.M. Parmentier (2000), The effects of deep damp melting on mantle flow and melt generation beneath mid-ocean ridges, *Earth and Planetary Science Letters*, 176, 339-356,
- Butler, R., T. Lay, K. Creager, P. Earl, K. Fischer, J. Gaherty, G. Laske, B. Leith, J. Park, M. Ritzwoller, J. Tromp, and L. Wen (2004), The Global Seismographic Network Surpasses Its Design Goal, *Eos*, 85(23), 225-229,
- Canales, J.P., R.S. Detrick, S. Bazin, A.J. Harding, and J.A. Orcutt (1998), Off-axis crustal thickness across and along the East Pacific Rise within the MELT area, *Science*, 280, 1218-1221,

- Darbyshire, F.A., I.T. Bjarnason, R.S. White, and O.G. Flovenz (1998), Crustal structure above the Iceland mantle plume imaged by the ICEMELT refraction profile, *Geophysical Journal International*, 135, 1131-1149,
- DeMets, C., R.G. Gordon, D.F. Argus, and S. Stein (1994), Effect of recent revisions to the geomagnetic reversal time scale on estimates of current plate motions, *Geophysical Research Letters*, 21(20), 2191-2194,
- Dunn, R.A., and D.W. Forsyth (2003), Imaging the transition between the region of mantle melt generation and crustal magma chamber beneath the southern East Pacific Rise with short-period Love waves, *Journal of Geophysical Research*, 108(7), 2352,
- Engdahl, E.R., R.D. Van der Hilst, and R.P. Buland (1998), Global teleseismic earthquake relocation with improved travel times and procedures for depth determination, *Bulletin of the Seismological Society of America*, 88, 722-743,
- Faul, U.H., and I. Jackson (2005), The seismological signature of temperature and grain size variations in the upper mantle, *Earth and Planetary Science Letters*, 234, 119-134,
- Fitton, J.G., A.D. Saunders, M.J. Norry, B.S. Hardarson, and R.N. Taylor (1997), Thermal and chemical structure of the Iceland Plume, *Earth and Planetary Science Letters*, 153, 197-208,
- Foulger, G.R., and D.G. Pearson (2001), Is Iceland underlain by a plume in the lower mantle? Seismology and helium isotopes, *Geophysical Journal International*, 145, F1-F5,
- Foulger, G.R., M.J. Pritchard, B.R. Julian, J.R. Evans, R.M. Allen, G. Nolet, W.J. Morgan, B.H. Bergsson, P. Erlendsson, S. Jakobsdottir, S. Ragnarsson, R. Stefansson, and K. Vogfjorð (2000), The seismic anomaly beneath Iceland extends down to the mantle transition zone and no deeper, *Geophysical Journal International*, 142, F1-F5,
- Gaherty, J. (2001), Seismic Evidence for Hotspot-Induced Buoyant Flow Beneath the Reykjanes Ridge, *Science*, 293, 1645-1647,
- Goldstein, P. (1996), SAC2000; seismic signal processing and analysis tools for the 21st century, *Seismological Research Letters*, 67(2),
- Gripp, A.E., and R.G. Gordon (2002), Young tracks of hotspots and current plate velocities, *Geophysical Journal International*, 150, 321-361,
- Hammond, W.C., and E.D. Humphreys (2000), Upper mantle seismic wave velocity: Effects of realistic partial melt geometries, *Journal of Geophysical Research*, 105(B5), 10975-10986,
- Hammond, W.C., and D.R. Toomey (2003), Seismic velocity anisotropy and heterogeneity beneath the Mantle Electromagnetic and Tomography Experiment (MELT) region of the East Pacific Rise from analysis of P and S body waves, *Journal of Geophysical Research*, 108, 2176,
- Hardarson, B.S., J.G. Fitton, R.M. Ellam, and M.S. Pringle (1997), Rift relocation: A geochemical and geochronological investigation of a palaeo-rift in northwest Iceland, *Earth and Planetary Science Letters*, 153, 181-196,

- Heller, D.-A., and G. Marquart (2002), An admittance study of the Reykjanes Ridge and elevated plateau between the Charlie-Gibbs and Senja fracture zones, *Geophysical Journal International*, *148*, 65-76,
- Hess, H.H. (1964), Seismic anisotropy of the uppermost mantle under oceans, *Nature*, *203*, 629-630,
- Hirth, G., and D.L. Kohlstedt (1996), Water in the oceanic upper mantle: implications for rheology, melt extraction and the evolution of the lithosphere, *Earth and Planetary Science Letters*, *144*, 93-108,
- Ito, G. (2001), Reykjanes 'V'-shaped ridges originating from a pulsing and dehydrating mantle plume, *Nature*, *411*, 681-684,
- Ito, G., J. Lin, and C.W. Gable (1996), Dynamics of mantle flow and melting at a ridge centered hotspot: Iceland and the Mid-Atlantic Ridge, *Earth and Planetary Science Letters*, *144*, 53-74,
- Ito, G., J. Lin, and D. Graham (2003), Observations and Theoretical Studies of the Dynamics of Mantle Plume-Mid-Ocean Ridge Interaction, *Reviews of Geophysics*, *41*(4), 3.1-3.24,
- Ito, G., Y. Shen, G. Hirth, and C.J. Wolfe (1999), Mantle flow, melting, and dehydration of the Iceland mantle plume, *Earth and Planetary Science Letters*, *165*, 81-96,
- Jones, S.M., N. White, and J. Maclennan (2002), V-shaped ridges around Iceland: Implications for spatial and temporal patterns of mantle convection, *Geochemistry Geophysics Geosystems*, *3*(10),
- Kaminski, E., and N.M. Ribe (2002), Timescales for the evolution of seismic anisotropy in mantle flow, *Geochemistry Geophysics Geosystems*, *3*, 1-17,
- Karato, S. (1993), Importance of anelasticity in the interpretation of seismic tomography, *Geophysical Research Letters*, *20*, 1623-1626,
- Keeton, J.A., R.C. Searle, B. Parsons, R.S. White, B.J. Murton, L.M. Parson, C. Peirce, and M.C. Sinha (1997), Bathymetry of the Reykjanes Ridge, *Marine Geophysical Researches*, *19*, 55-64,
- Lawver, L.A., and R.D. Muller (1994), Iceland hotspot track, *Geology*, *22*, 311-314,
- Li, A., and R.S. Detrick (2003), Azimuthal anisotropy and phase velocity beneath Iceland: implication for plume-ridge interaction, *Earth and Planetary Science Letters*, *6763*, 1-13,
- Montelli, R., G. Nolet, F.A. Dahlen, G. Masters, E.R. Engdahl, and S.-H. Hung (2004), Finite-frequency tomography reveals a variety of plumes in the mantle, *Science*, *303*, 338-343,
- Morgan, W.J. (1971), Convection plumes in the lower mantle, *Nature*, *230*, 42-43,
- Morgan, W.J. (1981), *Hotspot tracks and the opening of the Atlantic and Indian oceans*, The Sea, Wiley Interscience, New York.
- Murton, B.J., R.N. Taylor, and M.F. Thirwall (2002), Plume-Ridge Interaction: a Geochemical Perspective from the Reykjanes Ridge, *Journal of Petrology*, *43*(11), 1987-2012,
- Nataf, H.-C. (2000), Seismic Imaging of Mantle Plumes, *Annual Review of Earth and Planetary Science*, *28*, 391-417,

- Nishimura, C.E., and D.W. Forsyth (1988), The anisotropic structure of the upper mantle in the Pacific, *Geophysical Journal*, *96*, 203-209,
- Pilidou, S., K. Priestley, O. Gudmundsson, and E. Debayle (2004), Upper mantle S-wave speed heterogeneity and anisotropy beneath the North Atlantic from regional surface wave tomography: the Iceland and Azores plumes, *Geophysical Journal International*, *159*, 1057-1076,
- Poreda, R., J.G. Schilling, and H. Craig (1986), Helium and hydrogen isotopes in ocean-ridge basalts north and south of Iceland, *Earth and Planetary Science Letters*, *78*, 1-17,
- Ribe, N.M., U. Christensen, R., and J. TheiBing (1995), The dynamics of plume-ridge interaction, 1: Ridge-centered plumes, *Earth and Planetary Science Letters*, *134*, 155-168,
- Ritsema, J., H.J. Van Heijst, and J.H. Woodhouse (1999), Complex Shear Wave Velocity Structure Imaged Beneath Africa and Iceland, *Science*, *286*, 1925-1928,
- Saito, M. (1988) DISPER80: A subroutine package for the calculation of seismic normal-mode solutions, *Seismological Algorithms; Computational Methods and Computer Programs*, D.J. Doornbos, pp. 293-319.
- Scheirer, D.S., D.W. Forsyth, M.-H. Cormier, and K.C. Macdonald (1998), Shipboard geological indications of asymmetry and melt production beneath the East Pacific Rise near the MELT experiment, *Science*, *280*, 1221-1224,
- Schilling, J.G. (1973), Iceland mantle plume: Geochemical study of Reykjanes Ridge, *Nature*, *242*, 565-571,
- Schilling, J.G. (1985), Upper mantle heterogeneities and dynamics, *Nature*, *314*(62-67),
- Searle, R.C., J.A. Keeton, R.B. Owens, R.S. White, R. Mecklenburgh, B. Parsons, and S.M. Lee (1998), The Reykjanes Ridge: structure and tectonics of a hot-spot-influenced, slow-spreading ridge, from multibeam bathymetry, gravity, and magnetic investigations, *Earth and Planetary Science Letters*, *160*, 463-478,
- Smallwood, J.R., R.S. White, and T.A. Minshull (1995), Sea-floor spreading in the presence of the Iceland plume: the structure of the Reykjanes Ridge at 61°40'N, *Journal of the Geological Society of London*, *152*, 1023-1029,
- Talwani, M. (1971), Reykjanes ridge crest: A detailed geophysical study, *Journal of Geophysical Research*, *76*, 473,
- Talwani, M., J.L. Worzel, and M. Landisman (1959), Rapid gravity computations for two-dimensional bodies with application to the Mendocino submarine fracture zone, *Journal of Geophysical Research*, *64*, 49-59,
- Tarantola, A. (1987), *Inverse Problem Theory*, Elsevier, Amsterdam.
- Taylor, R.N., M.F. Thirwall, B.J. Murton, D.R. Hilton, and M.A.M. Gee (1997), Isotopic constraints on the influence of the Icelandic plume, *Earth and Planetary Science Letters*, *148*, E1-E8,
- Toomey, D.R., W.S.D. Wilcock, J.A. Condor, D.W. Forsyth, J.D. Blundy, E.M. Parmentier, and W.C. Hammond (2002), Asymmetric mantle dynamics in the MELT region of the East Pacific Rise, *Earth and Planetary Science Letters*, *200*, 287-295,

- Toomey, D.R., W.S.D. Wilcock, S.C. Solomon, W.C. Hammond, and J.A. Orcutt (1998), Mantle Seismic Structure Beneath the MELT Region of the East Pacific Rise from P and S Wave Tomography, *Science*, 280, 1224-1227,
- Vogt, P.R. (1971), Asthenosphere motion recorded by the ocean floor south of Iceland, *Earth and Planetary Science Letters*, 13, 153-160,
- Vogt, P.R. (1976), Plume, subaxial pipe flow, and topography along the mid-ocean ridges, *Earth and Planetary Science Letters*, 29, 309-325,
- Webb, S., C., and D.W. Forsyth (1998), Structure of the upper mantle under the EPR from waveform inversion of regional events, *Science*, 280, 1227-1229,
- White, R.S. (1997), Rift-plume interaction in the North Atlantic, *Philosophical Transactions of the Royal Society*, 355, 319-339,
- White, R.S., J.W. Brown, and J.R. Smallwood (1995), The temperature of the Iceland plume and origin of outward propagating V-shaped ridges, *Journal of the Geological Society of London*, 152, 1039-1045,
- White, R.S., and D. McKenzie (1989), Magmatism at rift zones; the generation of volcanic continental margins and flood basalts, *Journal of Geophysical Research*, 95, 7685-7729,
- Whitmarsh, R.B., and A.J. Calvert (1986), Crustal structure of the Atlantic fracture zones--I. The Charlie-Gibbs Fracture Zone, *Geophysical Journal of the Royal Astronomical Society*, 108, 16-34,
- Wolfe, C.J., I.T. Bjarnason, J.C. VanDecar, and S.C. Solomon (1997), Seismic structure of the Iceland mantle plume, *Nature*, 385, 245-247,
- Xue, M., and R.M. Allen (2005), Asthenospheric channeling of the Icelandic upwelling: Evidence from seismic anisotropy, *Earth and Planetary Science Letters*, 235, 167-182,
- Yale, M.M., and J. Phipps Morgan (1998), Asthenosphere flow model of hotspot-ridge interactions: a comparison of Iceland and Kerguelen, *Earth and Planetary Science Letters*, 161, 45-56,
- Yomogida, K., and K. Aki (1985), Waveform Synthesis of Surface Waves in a Laterally Heterogeneous Earth by the Gaussian Beam Method, *Journal of Geophysical Research*, 90(9), pp.7665-7688,
- Zhang, Y.-S., and T. Lay (1999), Evolution of oceanic upper mantle structure, *Physics of the Earth and Planetary Interiors*, 114, 71-80,
- Zhao, D. (2004), Global tomographic images of mantle plumes and subducting slabs: insight into deep Earth dynamics, *Physics of the Earth and Planetary Interiors*, 146, 3-34,